
FAR INFRARED ABSORPTION
IN SUPERCONDUCTORS

C

6

PHONON-INDUCED FAR INFRARED ABSORPTION
IN SUPERCONDUCTORS

By

Brian Farnworth, B.Sc.

A Thesis

Submitted to the School of Graduate Studies
in Partial Fulfilment of the Requirements
for the Degree
Doctor of Philosophy

McMaster University

January, 1976



DOCTOR OF PHILOSOPHY
(Physics)

McMASTER UNIVERSITY
Hamilton, Ontario

TITLE: Phonon-Induced Far Infrared Absorption
in Superconductors

AUTHOR: Brian Farnworth, B.Sc. (Simon Fraser University)

SUPERVISOR: Dr. T. Timusk

NUMBER OF PAGES: vii, 77

ABSTRACT: Phonon induced absorption spectra are presented for a variety of superconductors and compared to phonon densities of states derived from tunneling and neutron scattering experiments. Good signal to noise ratios permit differentiation of the spectra and thereby a direct presentation of the phonon spectrum. A simple weak coupling theory is used to interpret the results. For lead the simple theory is sufficiently accurate to permit inversion of the experimental spectrum to give a phonon density of states which contains fine structure that is in good agreement with neutron, but not tunneling, results. Evidence is found of phonon lifetime effects associated with the superconducting transition. A comparison is made with the full strong coupling theory, but only for the undifferentiated data, showing good agreement. In other materials phonon induced structure is weaker and in poorer agreement with the simple theory.

TABLE OF CONTENTS

		<u>Page</u>
CHAPTER I	INTRODUCTION	1
CHAPTER II	THEORY	5
	1. General Theory	6
	2. The Low q Limit	8
	3. The High q Limit	10
	4. Surface Absorption	11
	5. Phonon Induced Absorption	14
CHAPTER III	EXPERIMENT	17
	1. General Introduction	17
	2. Optics and Electronics	18
	3. Reflectivity Measurements	22
	4. Direct Absorption Measurements and He ³ Cryostat	24
	5. Sample Preparation	32
CHAPTER IV	RESULTS AND DISCUSSION	33
	1. Lead Foil	33
	2. Lead Film	43
	3. Comparison to Strong Coupling Theory	46
	4. Indium	49
	5. Niobium	53

	<u>Page</u>
CHAPTER IV	
6. Mercury	55
7. Nb ₃ Sn	55
8. Breakdown of the Simple Theory	58
CHAPTER V	
CONCLUSIONS	63
APPENDIX	
ERRORS AND NOISE	65
1. Electrical Noise	66
2. Lamp Fluctuations	67
3. Stepping Errors	68
4. Signal Averaging	72
5. Total Noise	74
BIBLIOGRAPHY	76

LIST OF FIGURES

<u>Figure</u>		<u>Page</u>
1.	Block diagram of apparatus	21
2.	Cavity for reflectivity measurements	23
3.	He ³ cryostat	25
4.	Sample and detector for direct absorption measurements	26
5.	Operating characteristics of He ³ cryostat	29
6.	Absorption spectrum of Pb foil compared to calculation based on tunneling density of states	34
7.	Absorption spectrum of Pb foil compared to calculation based on neutron density of states.	36
8.	Phonon density of states for Pb; Far infrared compared to tunneling	39
9.	Phonon density of states for Pb; Far infrared compared to neutron	40
10.	Absorption spectrum for a Pb-In alloy compared to pure Pb	42
11.	Absorption spectrum of Pb film showing splitting of the phonon peaks due to the double gap.	44

<u>Figure</u>		<u>Page</u>
12.	Absorption spectrum for Pb compared to strong coupling theory	48
13.	Absorption spectrum for In compared to a calculation based on neutron density of states	50
14.	Absorption spectrum for In compared to calculation based on tunneling density of states	51
15.	Tunneling and neutron derived phonon densities of states for In	52
16.	Absorption spectrum for Nb	54
17.	Absorption spectrum for Hg	56
18.	Absorption spectrum for Nb ₃ Sn.	57
19.	Frequency shift vs strong coupling parameter	59
20.	Frequency shift vs reduced frequency	62
21.	Effect of stepping errors on a spectrum	71

ACKNOWLEDGEMENTS

I would like to thank my supervisor, Dr. T. Timusk for his help, guidance and good humour throughout the course of this work and Dr. J. P. Carbotte for many helpful and encouraging discussions. The cooperation of John Neimanis and Peter Brewster, in the early experiments, is also gratefully acknowledged.

The samples of niobium were generously provided by Dr. J. M. Rowell and Dr. R. C. Dynes.

I am also grateful to Mrs. M. Pope for typing the manuscript.

Finally, I must thank my wife, Barbara, for her help in preparing and editing the manuscript as well as for her other, less tangible, contributions.

CHAPTER I
INTRODUCTION

The primary feature in the far infrared absorption spectrum of a superconductor is the energy gap. Photons of energy less than 2Δ cannot break Cooper pairs and so cannot be absorbed by the superconducting electrons. The absorptivity of a superconductor is therefore zero below the gap energy and approaches the normal metal value at high frequency ($\hbar\omega \gg 2\Delta$) where the effect of the superconducting transition on the electron energies is negligible. Initial calculations of the absorptivity by Mattis and Bardeen (1958) using BCS theory were in good general agreement with experiments by Glover and Tinkham (1957) which showed this behaviour.

Subsequent experiments (Richards and Tinkham 1960; Palmer and Tinkham 1968; Norman 1968; and others) showed deviations from the Mattis and Bardeen results for strong coupling superconductors. These deviations were partly the result of the assumption of BCS superconductivity and partly due to the assumption of the Pippard limit, i.e. the limit of very large wave vector, $q \gg 1/\xi$, where ξ is the superconducting coherence length. Nam (1967) carried out calculations

incorporating strong coupling effects, but still in the Pippard limit, and Ginsberg (1966) calculated the absorption, taking into account the wave vector dependence, but still using weak coupling theory. Ginsberg's calculations partly reproduced the extra absorption, relative to Mattis and Bardeen, observed just above the gap energy. Nam's calculations predicted weak structure on the absorption edge which was subsequently observed in lead by Joyce and Richards (1970), Gavini and Timusk (1971), and Brandli and Sievers (1972). This structure, as it comes from strong electron-phonon coupling effects, is a reflection of the phonon density of states on the electron energies. Finally Swihart and Shaw (1971) correctly combined the theory of strong coupling superconductivity and the anomalous skin effect to predict both the steepness of the absorption edge and the overall shape of the observed peaks, but not the fine structure pointed out by Gavini and Timusk.

The present work examines this phonon induced structure in lead in detail and extends the experiments to other materials. A major improvement over previous work is an increased signal to noise ratio which permits differentiation of the experimental spectrum and, thereby, a more direct presentation of the phonon spectrum.

In analysing the data the full theory of Swihart and Shaw is of limited value for two reasons. Firstly, the calculation has not been carried out in sufficient detail to permit a comparison of the derivative of the absorptivity.

Secondly, the calculation has so far been tied to lead and, furthermore, to the phonon density of states derived from tunneling experiments (McMillan and Rowell 1969). Fortunately an alternate theory exists which, though not always quantitatively correct, reproduces qualitatively the essential features of the observed spectra and is both easily understood and easily computed.

This theory, due to Allen (1970), again starts with BCS, but introduces the electron-light and electron-phonon couplings as perturbations. The first of these reproduces the results of Mattis and Bardeen. The second gives analytic expressions for the phonon induced absorption which are of great value in the interpretation of the experimental results. Despite its weaknesses, this simple theory agrees sufficiently well with the experiment, in the case of lead, to permit inversion of the data to give a phonon density of states. The density of states is found to be much more structured than that indicated by tunneling experiments; most of the observed structure is in good agreement with that found by inelastic neutron scattering (Stedman et al 1967). An additional peak, not present in either neutron or tunneling results, corresponding to phonons of energy of about 2Δ , is interpreted in terms of phonon lifetime effects associated with the superconducting transition.

Phonon induced absorption spectra in other systems are also presented. In mercury only weak structure is observed, primarily because of experimental problems introduced by the

4

sample being liquid at room temperature. In indium and niobium the structure is again weak because of the weaker electron-phonon coupling in these materials. Analysis of the data is made more difficult than in lead because of a breakdown of the simple theory for these metals, despite the fact that the weak coupling approximation is more appropriate. Structure is seen in Nb_3Sn but only to a limited extent, because of the poor quality of the samples.

CHAPTER II

THEORY

An exact calculation of the absorptivity of a metal requires a knowledge of the response of the metal to electric fields of all frequencies and all wavevectors. The form of such a calculation is outlined in section 1 of this chapter. The full calculations for superconducting lead, as carried out by Swihart and Shaw (1971), closely follow this programme and are quite exact, but since they are tied to lead and are exceedingly complicated they are of little value in the interpretation of the experimental results. The theory due to Allen (1970), on the other hand, makes a considerable simplification by treating the total absorption as the sum of contributions from two limits of the general theory, those of very large and very small wave vector. In sections 2 and 3 these two limits are discussed in general terms. In sections 4 and 5 Allen's derivations of expressions for these two contributions to the absorptivity are outlined. It is because these expressions are obtained in closed form that the simpler theory is so useful in interpreting the experimental results, even though the underlying assumptions of the theory cannot be justified.

1. General Theory of EM Absorption in a Metal

Consider a transverse electromagnetic wave incident on a metallic surface defined by $z=0$. Assuming normal incidence and plane polarization, the electric and magnetic fields at the surface of the metal are then:

$$(1) \quad \vec{E} = E_{x0} e^{-i\omega t} \hat{x}$$

$$(2) \quad \vec{H} = H_{y0} e^{-i\omega t} \hat{y}$$

Within the medium, E , H , and the induced current J are related by Maxwell's equations which become:

$$(3) \quad \frac{\partial}{\partial z} E_x(z,t) = -\frac{1}{c} \frac{\partial}{\partial t} H_y(z,t)$$

$$(4) \quad \frac{\partial}{\partial z} H_y(z,t) = -\frac{4\pi}{c} J_x(z,t)$$

Here it is assumed that the metal is isotropic, so that J is parallel to E and that the displacement current is negligible in comparison to J .

Eliminating H from equations (3) and (4)

$$(5) \quad \frac{\partial^2}{\partial z^2} E_x(z,t) = \frac{4\pi}{c} \frac{\partial}{\partial t} J_x(z,t)$$

and using equation (1) to eliminate the time dependence:

$$(6) \quad \frac{\partial^2}{\partial z^2} E_x(z) = -\frac{4\pi i\omega}{c^2} J_x(z)$$

The surface impedance is defined as the ratio of the electric and magnetic fields at the surface.

$$(7) \quad Z = \frac{4\pi}{c} \frac{E_{x0}}{H_{y0}}$$

By integrating equation (4) to give H_{y0} :

$$(8) \quad Z = E_{x0} / \int_0^{\infty} J_x(z) dz$$

The absorptivity is related to Z by:

$$(9) \quad A = \frac{c}{\pi} \text{Re}(Z)$$

Thus calculation of the absorptivity involves solution of the differential equation (6), together with some relation, such as Ohm's law, between the current and electric field, and substitution in equations (8) and (9).

However, Ohm's law in the real space form,

$$(10) \quad \vec{J}(\vec{r}, t) = \sigma_0 \vec{E}(\vec{r}, t)$$

is only valid in the local limit, i.e. when the electric field varies appreciably only over distances large compared to the mean free path of the electrons. Also the period of oscillation of the field must be large compared to the electron relaxation time. In general, the current at any point in space and time depends not only on the value of the electric field at that point, but on the field at all points back along the path of the electrons contributing to the current at that point. Ohm's law is then replaced by a relation of the form;

$$(11) \quad \vec{J}(\vec{r}, t) = \int_{-\infty}^t dt' \int d\vec{r}' K(\vec{r}-\vec{r}', t-t') \vec{E}(\vec{r}', t')$$

The nature of the reflections of the electrons by the metal surface, whether specular or diffuse, must also be taken into account.

General calculations of the surface impedance following this programme have been carried out by Reuter and Sondheimer (1948) (hereafter denoted RS) to give, in the case of specular reflection

$$(12) \quad Z_s(\omega) = -\frac{8i\omega}{c^2} \int_0^\infty dq [q^2 - \frac{\omega^2}{c^2} \{1 + \frac{4\pi i}{\omega} \sigma(q, \omega)\}]^{-1}$$

and for the diffuse case

$$(13) \quad Z_d(\omega) = \frac{4\pi^2 i \omega}{c^2} \left[\int_0^\infty dq \ln \left(1 - \frac{\omega^2}{c^2 q^2} \{1 + \frac{4\pi i}{\omega} \sigma(q, \omega)\} \right) \right]^{-1}$$

Here $\sigma(q, \omega)$ is the wavevector and frequency dependent conductivity defined Ohm's law in Fourier space.

$$(14) \quad J(q, \omega) = \sigma(q, \omega) E(q, \omega)$$

2. The Low q Limit

In the local limit, where Ohm's law is valid, the q dependence of the conductivity can be ignored and the ω dependence taken into account by the Drude formula.

$$(15) \quad \sigma(\omega) = \frac{\sigma_0}{1 + i\omega\tau}$$

Here σ_0 is the DC conductivity and τ is the relaxation time which may be a function of frequency. This formula is valid for values of the mean free path (l) much shorter than a

wavelength of the applied field,

$$(16) \quad \lambda = v_f \tau \ll 1/q$$

where v_f is the Fermi velocity, and thus the local limit corresponds to small q contributions to the RS integrals.

Integration of either (12) or (13) with this model conductivity yields, in the low frequency or "classical skin effect" region,

$$(17) \quad A(\omega) = \left[\frac{2\omega}{\omega_p^2 \tau} \right]^{1/2}, \quad \omega \tau \ll 1$$

and in the high frequency limit, or "classical relaxation" region,

$$(18) \quad A(\omega) = \frac{2}{\omega_p \tau}, \quad \omega \tau \gg 1$$

where ω_p is the plasma frequency

$$(19) \quad \omega_p^2 = \frac{Ne^2}{m}$$

While equation (15) is true only for normal metals, its high frequency limit

$$(20) \quad \text{Re}[\sigma(\omega)] = \frac{\omega_p^2}{4\pi\omega} \frac{1}{\omega\tau}$$

has its equivalent in the case of phonon induced absorption in a superconductor, so equation (18) can be used for both normal and superconducting metals.

3. The Large q Limit

Drude theory is not adequate for a pure metal at low temperature where, to a first approximation, the metal behaves as a collisionless free electron gas. If, in the absorption of a photon of frequency ω and wave vector q , a free electron is scattered from state \vec{k} to \vec{k}' , energy and momentum conservation require

$$(21) \quad \hbar\omega = \frac{\hbar^2}{2m} (k^2 - k'^2)$$

$$\vec{q} = \vec{k} - \vec{k}'$$

Since we are interested in photon energies much less than the Fermi energy both k and k' are of the order of the Fermi momentum, and it is easily shown that equations (21) require

$$(22) \quad q > \frac{\omega}{v_f} .$$

In an interaction between a free electron and a free photon this condition is not satisfied since for the photon

$$(23) \quad q = \frac{\omega}{c} \ll \frac{\omega}{v_f} .$$

It is the exponential decay of the electric field in the surface layer of the metal that gives large q components of the field. Thus large q contributions to the RS integrals are known as the "surface absorption". In the event of a collision between the electron and a phonon or impurity, condition (21) is relaxed and absorption is

possible for low q . Low q absorption is then dependent more on the bulk properties of the metal than the existence of the surface and is called "volume" absorption.

The large q , or "extreme anomalous" limit, is defined, in the normal metal, by

$$(24) \quad q \gg 1/\lambda$$

but in the superconductor the role of the mean free path is filled by the coherence length and the analogous, or "Pippard" limit, is defined by

$$(25) \quad q \gg 1/\xi$$

In the case of lead this condition is not satisfied even in the purest samples (Swihart and Shaw, 1970), so the distinction between surface and volume absorptions is not rigorous. This is one major weakness of the simple theory.

4. Allen's Theory for the Surface Absorption

The real part of the conductivity can be calculated from the rate of energy dissipation by the electric field.

$$(26) \quad |E_x|^2 \text{Re}[\sigma(q, \omega)] = \hbar \omega P(q, \omega)$$

where $P(q, \omega)$ is the transition probability per unit time given by the golden rule

$$(27) \quad P(q, \omega) = \frac{2\pi}{\hbar} \sum_f |\langle f | H_{\text{ext}} | 0 \rangle|^2 \delta(E_f - E_0 - \hbar\omega)$$

The ground state $|0\rangle$ is the free Fermi sea or BCS ground state for the normal or superconducting metal respectively. The sum is over all excited states $|f\rangle$ of energy E_f .

The Hamiltonian for an electron in an external field is

$$(28) \quad H = \frac{1}{2m} (\vec{p} + \frac{e\vec{A}}{c})^2$$

where p is the electron momentum and A the vector potential of the applied field. Expanding (28) and neglecting the term that is quadratic in A

$$(29) \quad H = \frac{p^2}{2m} + \frac{e}{2c} (\vec{v} \cdot \vec{A} + \vec{A} \cdot \vec{v})$$

The second term is taken as the perturbation Hamiltonian and expressed in the second quantisation form by taking matrix elements between Bloch states

$$(30) \quad H_{\text{ext}} = \sum_{\vec{k}} \frac{e}{c} \vec{A} \cdot \vec{v}_{\vec{k}+\vec{q}/2} c_{\vec{k}+\vec{q}}^{\dagger} c_{\vec{k}}$$

where c^{\dagger} is the creation operator for a Bloch state of velocity $\vec{v}_{\vec{k}}$ and wavevector \vec{k} . \vec{q} is the wavevector of the applied electric field and the approximation has been made that

$$(31) \quad \frac{1}{2} \{ \vec{v}_{\vec{k}+\vec{q}} + \vec{v}_{\vec{k}} \} = \vec{v}_{\vec{k}+\vec{q}/2}$$

The electric field is given by

$$(32) \quad E = -\frac{1}{c} \frac{\partial A}{\partial t} = \frac{i\omega}{c} A$$

and, as in section 1, is assumed to lie in the x direction.

For the superconducting case the Hamiltonian must be expressed in terms of the creation and annihilation operators for BCS single particle excitations, γ^{\dagger} and γ , by means of the Bogoliubov-Valatin transformation. At zero temperature, where only terms with two quasiparticle creation

operators enter

$$(33) \quad H_{\text{ext}} = \sum_{\mathbf{k}} \frac{e}{c} \vec{A} \cdot \vec{v}_{\mathbf{k}+\mathbf{q}/2} p(\mathbf{k}, \mathbf{k}+\mathbf{q}) \gamma_{\mathbf{k}+\mathbf{q}}^+ \gamma_{-\mathbf{k}}^+$$

$p(\mathbf{k}, \mathbf{k}+\mathbf{q})$ is a coherence factor defined by

$$(34) \quad p^2(\mathbf{k}, \mathbf{k}') = \frac{1}{2} \left[\frac{1 - \epsilon_{\mathbf{k}} \epsilon_{\mathbf{k}'} + \Delta_{\mathbf{k}} \Delta_{\mathbf{k}'}}{E_{\mathbf{k}} E_{\mathbf{k}'}} \right]$$

$E_{\mathbf{k}}$ is the energy of an excitation of wavevector \mathbf{k} related to the free electron energy and the BCS gap parameter by

$$(35) \quad E_{\mathbf{k}}^2 = \epsilon_{\mathbf{k}}^2 + \Delta_{\mathbf{k}}^2$$

Combining equations (29) to (33) and evaluating the matrix elements gives the real part of the conductivity for normal and superconducting metals, respectively

$$(36) \quad \text{Re}[\sigma_{N,o}(q, \omega)] = \frac{\pi e^2}{\omega} \sum_{\mathbf{k}} v_{\mathbf{k}\mathbf{x}}^2 f_{\mathbf{k}} (1 - f_{\mathbf{k}+\mathbf{q}}) \delta(\hbar\omega - \epsilon_{\mathbf{k}+\mathbf{q}} + \epsilon_{\mathbf{k}})$$

$$(37) \quad \text{Re}[\sigma_{S,o}(q, \omega)] = \frac{\pi e^2}{\omega} \sum_{\mathbf{k}} v_{\mathbf{k}\mathbf{x}}^2 p^2(\mathbf{k}, \mathbf{k}+\mathbf{q}) \delta(\hbar\omega - E_{\mathbf{k}+\mathbf{q}} - E_{\mathbf{k}})$$

The subscript o denotes the collisionless gas contribution to the conductivity and f is the Fermi factor

$$(38) \quad f_{\mathbf{k}} = \frac{1}{e^{\epsilon_{\mathbf{k}}/k_B T} + 1}$$

These expressions for the real part of the conductivity are integrated and Kramers-Kronig transformed to give the imaginary part. The absorptivity is then evaluated from the RS integral expressions to give, for the normal metal

$$(39) \quad A_{N,o} = \sqrt{3} \left[\frac{4}{5\pi} \frac{v_f}{c} \frac{\omega}{\omega_p} \right]^{1/3}$$

and for the superconductor

$$(40) \quad A_{s,o} = A_{N,o} \operatorname{Re}[2e^{i\omega/3}/r(\omega)]$$

where

$$(41) \quad \operatorname{Re}[\tau(\omega)] = \begin{cases} 0 & \hbar\omega < 2\Delta \\ \frac{(1+2\Delta)}{\hbar\omega} E(\eta) - \frac{4\Delta}{\hbar\omega} K(\eta), & \hbar\omega > 2\Delta \end{cases}$$

$$\operatorname{Im}[\tau(\omega)] = \frac{1}{2} \frac{(1+2\Delta)}{\hbar\omega} E(\eta') - \frac{1}{2} \frac{(1-2\Delta)}{\hbar\omega} K(\eta')$$

Here K and E are complete elliptic integrals of the first and second kind and

$$\eta = \frac{\hbar\omega - 2\Delta}{\hbar\omega + 2\Delta}, \quad \eta' = (1 - \eta^2)^{1/2}$$

These results, which were first derived by Mattis and Bardeen (1958), give an absorptivity for the superconductor which is zero below the energy gap, 2Δ , and smoothly approaches the normal metal value at high frequencies.

5. Allen's Theory for Phonon Induced Absorption

The calculation of the phonon induced contribution to the absorptivity is analogous to the surface case but the golden rule must be taken to second order

$$(42) \quad P(q, \omega) = \frac{2\pi}{\hbar} \sum_f \sum_n \frac{|\langle f | H' | n \rangle \langle n | H' | o \rangle|^2 \delta(E_f - E_o - \hbar\omega)}{E_o - E_n}$$

The perturbation Hamiltonian includes both electron-light and electron-phonon Hamiltonians

$$(43) \quad H' = H_{\text{ext}} + H_{\text{ph}}$$

$$H_{\text{ph}} = \sum_{kk'} M_{kk'} C_k^+ C_k (a_Q + a_{-Q}^+)$$

a_Q^+ is the creation operator for a phonon of wavevector Q and energy $\hbar\Omega_Q$. $M_{kk'}$ is the matrix element for the scattering of an electron from Bloch state k to k' by a phonon.

The conductivity becomes

$$(44) \quad \sigma_{N,\text{ph}}^1 = \frac{2\pi e^2}{3\hbar^2 \omega^3} \sum_{kk'} |M_{kk'}|^2 (\vec{v} - \vec{v}')^2 f_k (1 - f_{k'}) \delta(\epsilon - \epsilon' + \hbar\Omega_Q - \hbar\omega)$$

$$\sigma_{S,\text{ph}}^1 = \frac{\pi e^2}{3\hbar^2 \omega^3} \sum_{kk'} |M_{kk'}|^2 (\vec{v} - \vec{v}')^2 \frac{1}{2} (1 - \frac{\epsilon\epsilon' - \Delta\Delta'}{EE'}) \delta(E + E' + \hbar\Omega_Q - \hbar\omega)$$

These expressions are simplified by introducing the quantity

$$(45) \quad \alpha_{\text{tr}}^2 F(\Omega) = \frac{N(o)}{4v_f^2} \langle\langle |M_{kk'}|^2 (\vec{v} - \vec{v}')^2 \delta(\hbar\Omega_Q - \hbar\Omega) \rangle\rangle$$

where $N(o)$ is the density of electron states at the Fermi surface and $\langle\langle \rangle\rangle$ denotes averaging over the Fermi surface.

The quantity $\alpha_{\text{tr}}^2 F(\Omega)$ is a phonon density of states, weighted by electron-phonon coupling strengths, analogous to the one that appears in the theory of strong coupling superconductivity

$$(46) \quad \alpha_o^2 F(\Omega) = \frac{N(o)}{2\hbar} \langle\langle |M_{kk'}|^2 \delta(\hbar\Omega_Q - \hbar\Omega) \rangle\rangle$$

The difference is that for calculation of transport properties additional weight is given to large angle scattering by the factor $(\vec{v}-\vec{v}')$ in equation (45).

The final expressions for the conductivity are of the high frequency Drude form, equation (20), with frequency dependent relaxation times given by

$$(47) \quad \frac{1}{\tau_{N,ph}} = \frac{2\pi}{\omega} \int_0^{\omega} d\Omega (\omega-\Omega) \alpha_{tr}^2 F(\Omega)$$

$$\frac{1}{\tau_{S,ph}} = \frac{2\pi}{\omega} \int_0^{\omega-2\Delta} d\Omega (\omega-\Omega) \alpha_{tr}^2 F(\Omega) E\left[1 - \left(\frac{2\Delta}{\omega-\Omega}\right)^2\right]^{\frac{1}{2}}$$

Here 2Δ is the superconducting energy gap and E is a complete elliptic integral of the second kind.

The absorptivity is then given by equation (18)

~~$$(48) \quad A = \phi(\omega) \frac{2}{\omega p \tau}$$~~

where the function $\phi(\omega)$, which is expected to be slowly varying, and of the order of 1 at high frequency, is included to partially compensate for the assumption

$$(49) \quad \omega \tau \gg 1$$

which is probably not valid at low frequencies.

CHAPTER III

EXPERIMENT

1. General Introduction

The absorptivities of various superconductors were measured by two techniques; indirectly, by detecting light reflected from the sample, and directly, by measuring the power absorbed by the sample by its temperature rise.

The reflectivity measurements had the advantages of being simple and requiring only a 1.2 K cryostat but had several disadvantages. Since the reflectivity of a metal in the far infrared is very close to one, only a small fraction of the light is absorbed even after many reflections. This means that the structure in the spectrum due to absorption in the metal is a small perturbation on a large background and, therefore, extremely sensitive to uncontrolled variations in the background. Thus, it was not possible to compare the spectrum of a superconductor to that of a normal metal taken in a separate experiment; the superconductor had to be driven normal "in situ" with a magnetic field. This was of course not possible in the case of Nb_3Sn and other high T_c superconductors. A further disadvantage of the reflectivity technique is the requirement of large samples to line a reflecting cavity.

These difficulties were at least partially overcome in the second technique. Here the power absorbed was detected directly by means of a bolometer attached to the back of the sample and outside the direct radiation beam. The sample could be small (~ 1 cm diameter) but had to be in the form of a thin foil ($\sim 100\mu$). Since the whole, rather than just a small part, of the signal was due to light absorbed in the sample, the sensitivity to changes in the background spectrum was greatly reduced. Thus, comparison of spectra taken on different days became possible. However, the need for an extremely sensitive detector dictated lower temperatures and a He^3 cryostat.

2. Optics and Electronics

Measurements were made with Michelson and Lamellar grating interferometers over the spectral ranges 30 to 350 cm^{-1} and 10 to 50 cm^{-1} respectively.

The Michelson interferometer used is basically a commercial instrument (RIIC FS720) with two major modifications. Firstly, the original mirror drive has been replaced by a more accurate drive stage (Aerotech ATS-301-M-D) with a stepping motor (Slo-Syn HS25V). A discussion of mirror inaccuracies is included in the Appendix.

Secondly, the option of dual beam operation has been included. This modification has been described in detail by Douglas and Timusk (1974) and is designed to minimize noise due to fluctuations in lamp intensity. Light is allowed

through the upper and lower halves of the interferometer alternately by a half-moon shaped chopper blade. In the upper beam the moving mirror is shadowed by a fixed mirror located to form an interferometer at large fixed path difference. The lower beam forms the interferometer proper. The resulting signal at the detector is then a combination of signals from the actual and reference interferometers, 180° out of phase. When the signal is fed into a lock-in amplifier with a reference signal at the chopper frequency, the output is the difference of the signals from the two beams. The reference mirror is adjusted to give a null signal when the moving mirror is at a position of large path difference. In this way the large DC background is subtracted from the interferogram.

The reference signal for the lock-in amplifier is supplied by a phototransistor which detects light, from a light emitting diode, reflected by a mirror attached to the shaft of the chopper motor. The phototransistor and LED are mounted on an arm that can be rotated, from outside the interferometer, concentrically with the chopper motor. This enables the phase of the reference signal to be adjusted simply and over a wide range, even while the interferometer is under vacuum. The chopper is driven by a hysteresis type synchronous motor with a variable frequency power supply to permit chopper frequencies over the range 5 to 20 Hz.

The Lamellar interferometer is again a commercial instrument (Beckman LR100) and has been described in detail

by Chantry (1971). The only modification here is the inclusion of a double beam chopping system similar to that in the Michelson.

Both instruments use a UA-2 type mercury arc lamp with a fused quartz envelope. All light of frequency greater than 380 cm^{-1} is filtered out by black polyethylene at the exit aperture of the interferometer and sapphire at 1.2 K just before the detector. In addition the Lamellar is operated with an interference filter that eliminates the rest of the light above 100 cm^{-1} . The interferometers are maintained under a vacuum of 10^{-4} Torr by liquid nitrogen cooled adsorption pumps.

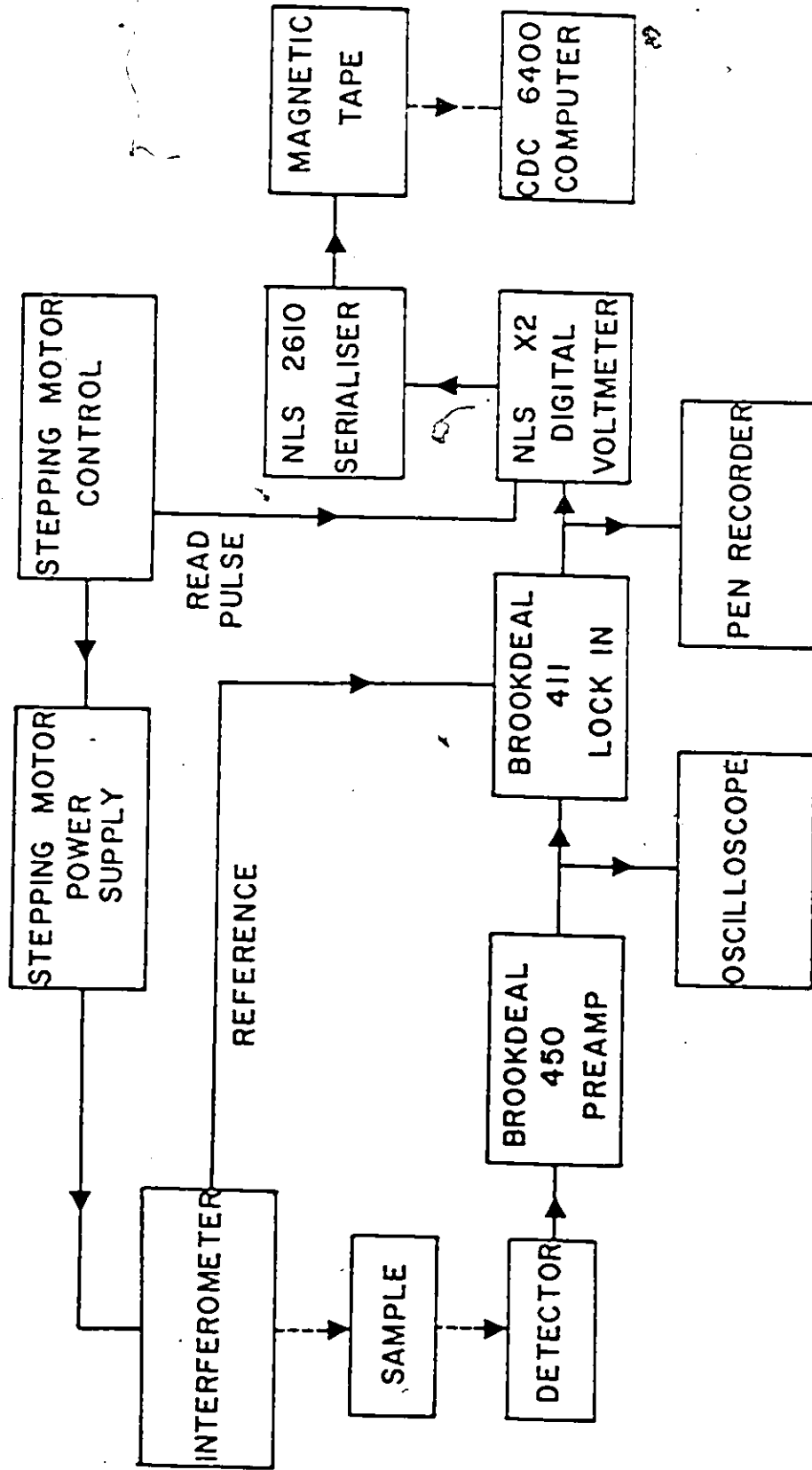
The detectors are doped germanium bolometers for use at 1.2 K (Tumber 1969), or 0.3 K (Drew and Sievers 1971).

A block diagram of the apparatus is shown in figure (1). The bolometer signal is amplified by a Brookdeal 450 low noise preamplifier and averaged by a Brookdeal 411 lock-in amplifier with a time constant of typically 1 second. The output signal is measured by a Non-linear Systems X-2 digital voltmeter and recorded, via a NLS 2610 serializer, on magnetic tape for later analysis on a CDC 6400 computer.

The stepping motor control drives the mirror rapidly (at 300 steps/s) through a series of steps and gives a read signal to the DVM 100 ms before the next series. The interval between each series of steps is typically 1 s. Each step corresponds to a path difference change of 5μ (unfortunately 5.08μ in the Michelson) giving a frequency

FIGURE 1

Block diagram of the experimental apparatus



cutoff of 125, 250, or 500 cm^{-1} with 2, 4, or 8 steps per data point.

3. Reflectivity Measurements

Reflectivity measurements were performed on evaporated films of Pb, foils of Pb and Pb-In alloys, and bulk samples of Hg. Figure (2) shows the cavity employed for film measurements. The sample is evaporated onto the walls of a non-resonant conical cavity machined from stainless steel. Light is fed into the cavity through a polished brass light pipe and condensing cone. The light exits, after an average of about 100 reflections from the sample, through a sapphire filter to the detector. A small superconducting solenoid, capable of providing a field of a few kilogauss, is wound around the cavity to drive the sample normal. The whole assembly is immersed in a pumped He^4 cryostat at 1.2 K.

For foil measurements the conical cavity is replaced by a cylinder lined with the foil and for measurements on Hg a hemispherical cavity is used with a pool of Hg forming the flat surface.

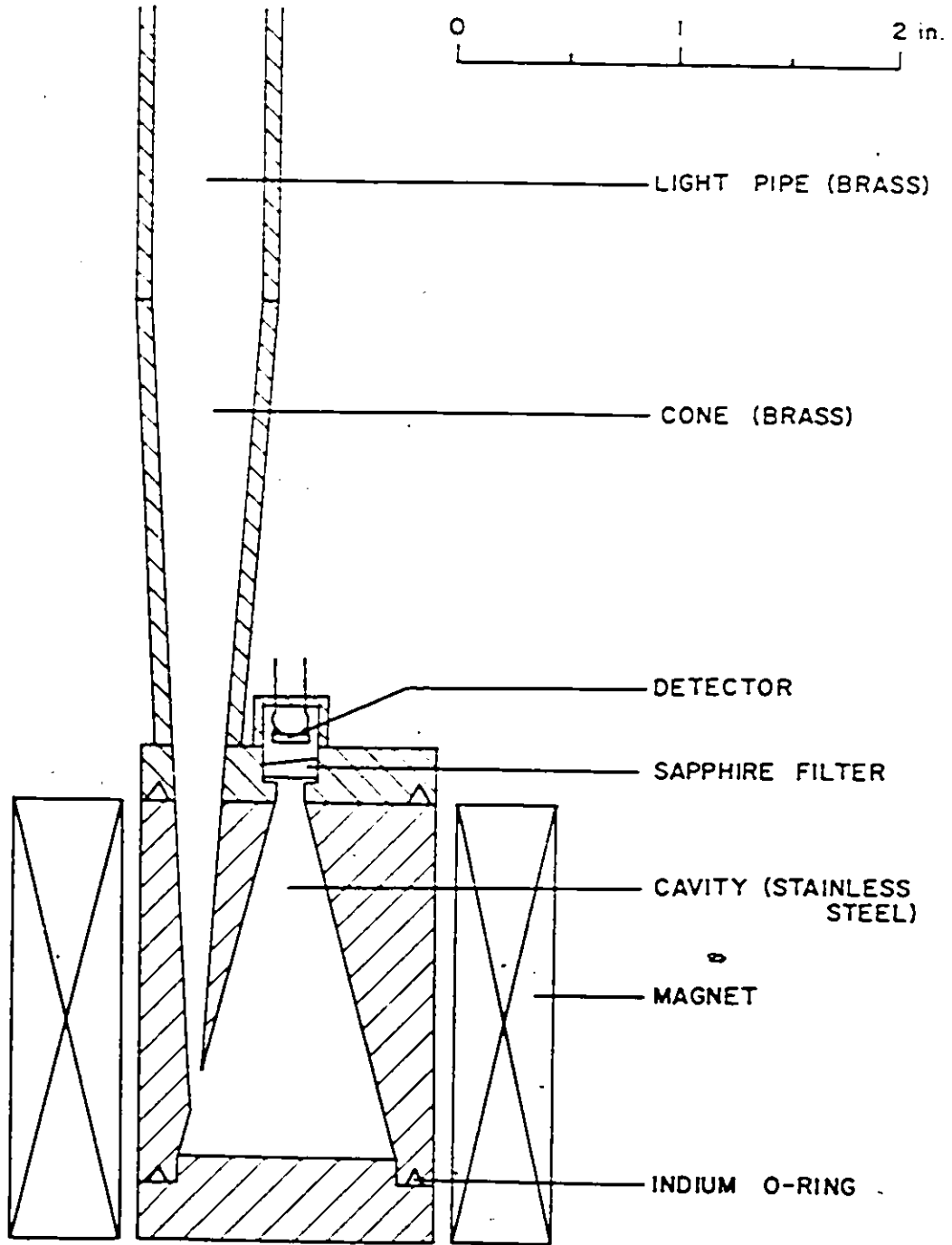
The measured quantity is the ratio of the light intensity reaching the detector with the sample in the superconducting state to that in the normal state.

$$\begin{aligned}
 (50) \quad S(\omega) &= I_S(\omega)/I_N(\omega) \\
 &= \left[\frac{1-A_S(\omega)}{1-A_N(\omega)\omega} \right]^n = 1-n \{A_S(\omega)-A_N(\omega)\}
 \end{aligned}$$

where A_S and A_N are the absorptivities of the superconducting.

FIGURE 2

The cavity used for reflectivity measurements on lead films. The sample is evaporated onto the inside surface of the cavity which is then sealed onto the light pipe-detector assembly with indium O-rings. A small superconducting magnet is used to drive the sample normal. Different cavities are used for foils of lead and lead-indium alloys and for bulk samples of mercury.



and normal metals and n is the average number of reflections. The approximation is valid for $nA \ll 1$ and typically $nA = 0.1$.

Assuming photons travel from the entrance to the exit apertures in a random walk, the average number of reflections can be calculated from the absorptivity of the sample walls

$$(47) \quad n = \sum a_i / \sum a_i A_i$$

where A_i is the absorptivity of a section of the wall of area a_i . Since the sum in the denominator is dominated by the entrance and exit holes, n does not depend appreciably on frequency, or on whether the sample is superconducting or normal.

Signal strengths in these experiments were about 0.5 mV with noise levels of the order of 0.1%. Twenty to thirty scans were averaged together to further reduce the noise, superconducting and normal scans being alternated to eliminate the effects of changes in spectral shape with time.

4. Direct Absorption Measurements - He³ Cryostat

The He³ cryostat used for absorption measurements is shown in figure (3) and the sample chamber is shown in detail in figure (4). The cryostat is designed to fit inside a 4 in. diameter glass He⁴ dewar and be completely self-contained, requiring no external pumping system.

At the top of the cryostat is a storage chamber which contains 80% of the He³ gas at room temperature. This is directly connected via a 1/4 in. diameter tube to the He³

FIGURE 3

The He^3 cryostat used for direct absorption measurements. At room temperature most of the He^3 gas is contained in the storage chamber and the valve is closed, isolating the charcoal adsorption pump. At 1.2 K the He^3 has condensed and dripped down into the liquid can contained inside the sample chamber. The valve is then opened and the He^3 pumped down to 0.3 K. The He^3 is permanently contained inside the cryostat.

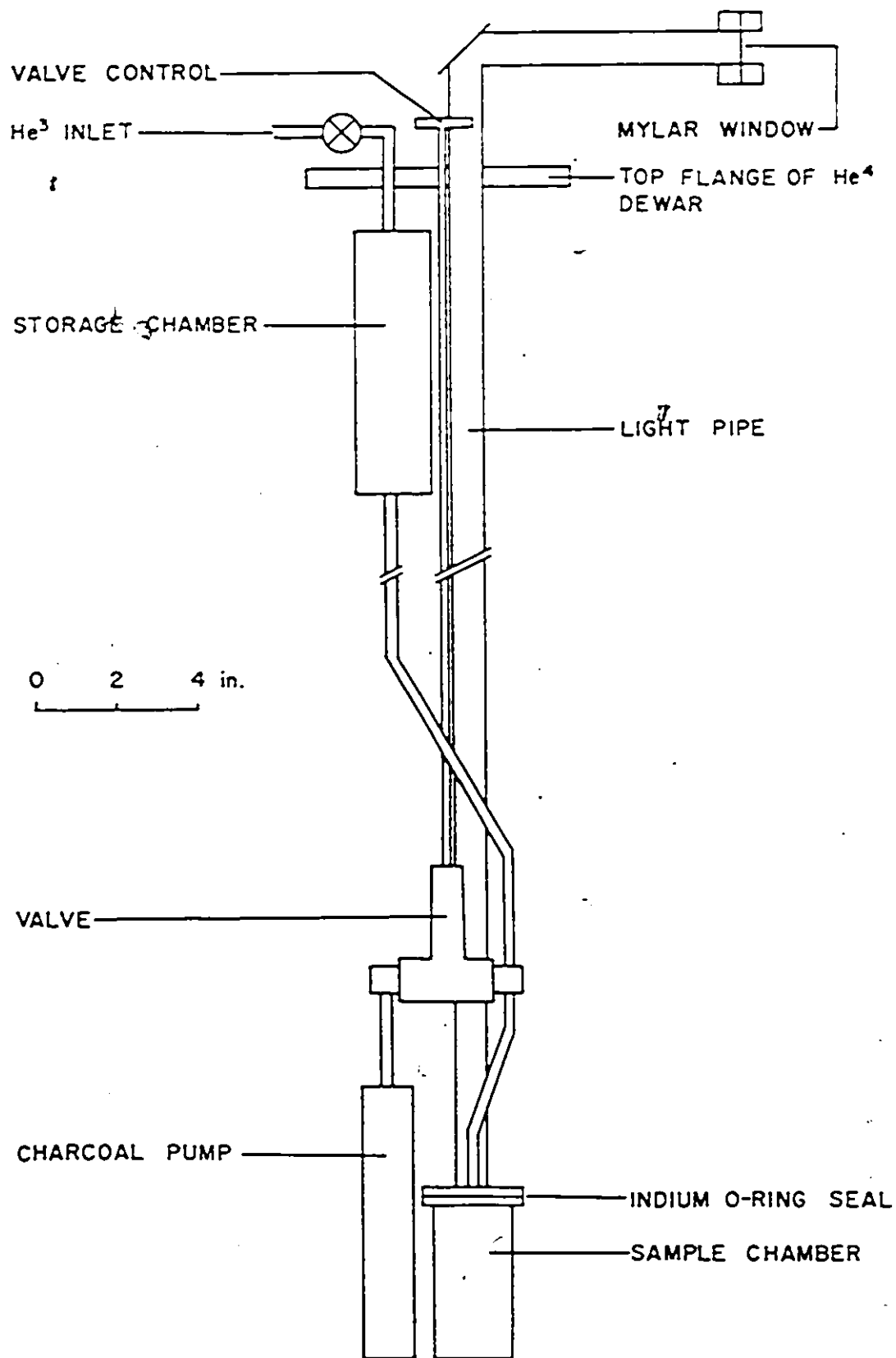
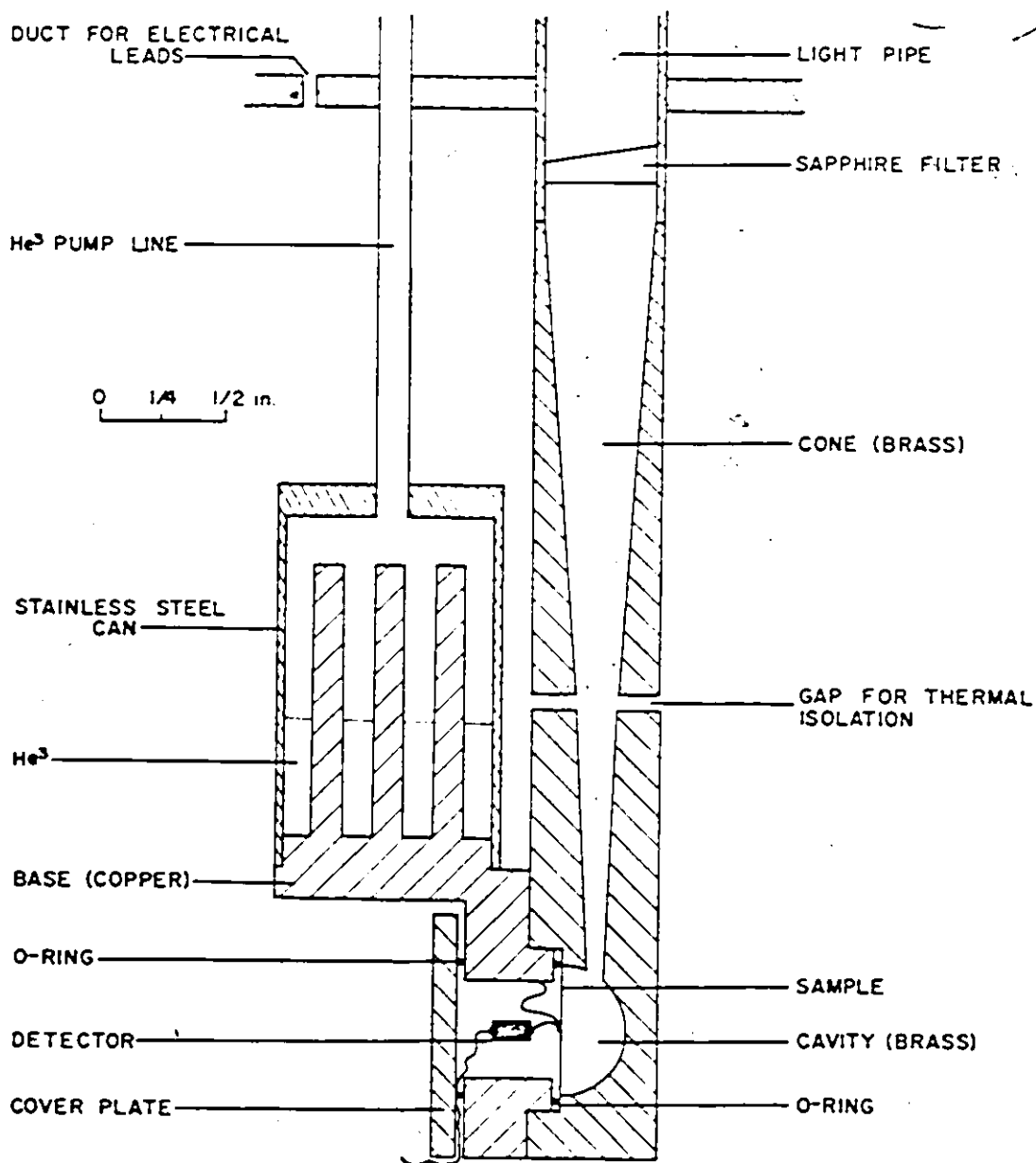


FIGURE 4

Interior of the sample chamber of the He³ cryostat. The sample, a thin foil, forms the flat surface of a hemispherical cavity. The detector, which is soldered to the rear surface of the sample and is outside the direct radiation beam, measures the temperature rise of the sample due to the absorption of radiation. The sample and detector are weakly thermally coupled to the base of the He³ liquid can by a copper wire.



liquid can which is contained in the vacuum of the sample chamber. This can is a stainless steel cylinder with a copper base on which the sample is mounted. The base is machined from a solid piece of copper with fingers extending up into the can to provide good thermal contact with the He³ liquid. The only mechanical contact between the liquid can and the walls of the sample chamber is via the He³ pumping line made of 1/4 in. thinwall stainless steel tubing and, negligibly, by three 0.003 in. diameter constantan wires to the detector and thermometer. A calibrated carbon resistor (Speer 470Ω) is mounted on the copper base to act as a thermometer.

The He³ is pumped by a charcoal adsorption pump connected to the liquid can by about 8 in. of 1/4 in. diameter tubing through a 1/4 in. bellows valve (Nupro SS-4UW-SW) which can be operated from outside the cryostat. The pump contains 40 gm of activated charcoal loosely packed between two concentric cylinders of copper mesh. This arrangement is to provide direct access for the gas to as much of the charcoal surface as possible.

Radiation from the interferometer is fed to the sample chamber through a polished brass light pipe with a sapphire filter at the entrance to the sample chamber. The sapphire excludes most of the room temperature radiation from the top of the light pipe which would otherwise put an excessive heat load on the cryostat. The sample chamber and light pipe form a common vacuum space maintained at the room temperature end of the light pipe by a mylar window. This

arrangement eliminates the need for a low temperature window.

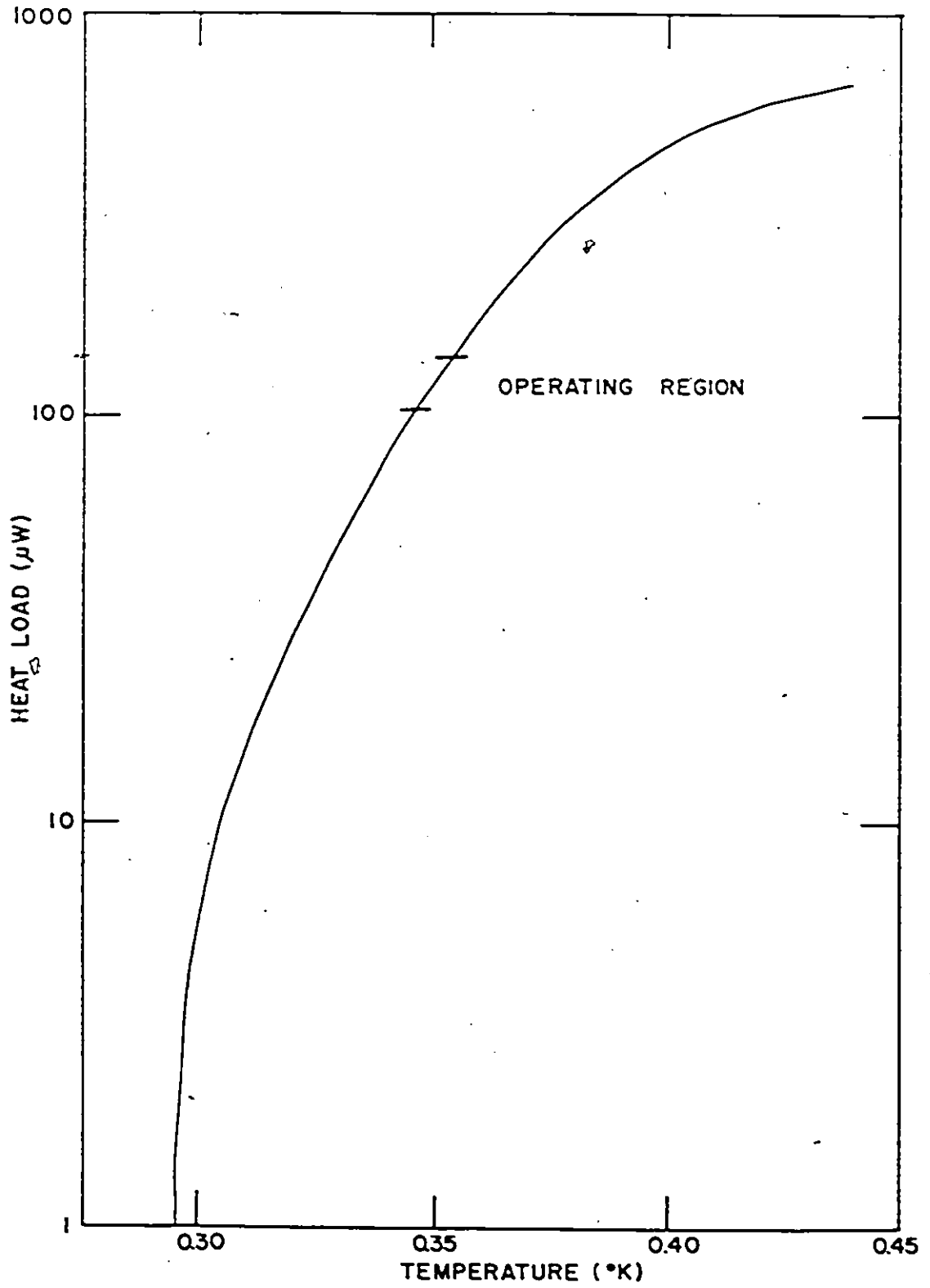
Electrical leads pass through a 1/8 in. diameter stainless steel tube from the sample chamber to a vacuum feed-through at the top of the cryostat. The leads are thermally anchored to the walls of the sample chamber to prevent significant thermal contact between the He³ can and the top of the cryostat.

Operation of the cryostat is as follows. At room temperature, with most of the He³ gas in the storage chamber, the valve is closed isolating the charcoal pump. A few Torr of hydrogen exchange gas is admitted to the sample chamber and the system is precooled with liquid nitrogen. He⁴ is then transferred slowly enough that the liquid can remains essentially in thermal equilibrium with the He⁴ bath. Thus when the H₂ exchange gas freezes out, at about 10 K, the liquid can is not at significantly higher temperature. The He⁴ dewar is then rapidly filled and pumped down to 1.2 K. Cooling of the liquid can then continues due to He³ condensing in the pumping line and dripping down into the liquid can. When the liquid has cooled to 1.2 K the valve is opened and the He³ is pumped down to the operating temperature in about 5 min.. The whole cooling process, from room temperature to 0.35 K, takes 1 to 1 1/2 hours.

The temperature versus heat load characteristics of the cryostat with the light pipe blocked off are shown in figure (5). The ultimate temperature reached was 0.29 K with a base heat load of about 10 μ W. The thermal conduction along the pumping line was estimated to be 4 μ W, the rest of the heat

FIGURE 5

Characteristics of the He cryostat. The ultimate temperature reached was 0.29 K. Under operating conditions a 100 μ W heat load is caused by radiation down the light pipe, raising the temperature to about 0.35 K. A 32 STP charge of He gives a holding time of 6 to 8 hours.



load coming from conduction by the He^3 gas. The operating temperature was 0.35 K which indicates a radiation load of 100 μ W. The pumping speed is about 20 cm^3/s at the ultimate temperature.

The favourable features of this cryostat are its simplicity and reliability. All components, except the light pipe and the base to the liquid can, are of stainless steel. The joints are welded whenever possible, or otherwise hard soldered. Thus the only joint likely to fail is the indium O-ring sealing the cover to the sample chamber. The absorption pump eliminates long, carefully baffled, pumping lines to an external vacuum system and, since the He^3 gas is permanently contained inside the cryostat, there is little risk of its loss or contamination. A disadvantage of the system is the need to warm up the whole cryostat to 50 K to recondense the He^3 after it has all been absorbed on the charcoal. However, a 3 ℓ STP charge of He^3 gives a holding time of 6 to 8 hours under operating conditions, so this drawback is not serious.

The arrangement of the sample and detector can be seen in figure (4). The front surface of the sample forms the flat surface of a hemispherical brass cavity. The detector is indium soldered to the back surface. Radiation is fed into the cavity by a condensing cone. Approximately 1% of the light is absorbed in the sample causing its temperature, and hence that of the bolometer, to rise. In order for the sample temperature to follow the intensity of the chopped radiation, the sample must be weakly coupled thermally to the base of

the He^3 can. This coupling is provided by a 0.02 in. diameter copper wire about 1/2 in. long. Both the ambient temperature of the detector, and hence its sensitivity, and the thermal time constant of the sample depend on the strength of this coupling. Therefore, the thickness of the wire is adjusted, by trial and error, to give maximum signal with a chopping frequency of 10 Hz. The thermal time constant varies from sample to sample over the range 10 to 100 ms. Signal strengths are in the range 0.2 to 2 mV RMS.

Light is prevented from reaching the detector by leakage around the edges of the sample by means of an O-ring made from 0.030 in. diameter electrical solder. The initial, more obvious, choice of indium as an O-ring material was rejected since it provided too much thermal conduction between the sample and its mount. Another choice, copper, also works well but requires inconveniently large forces to be squeezed flat. Without the O-ring in place, despite the fact that the crack between the sample and the mount is much less than a wavelength, signal strengths due to leaked radiation are ten times those due to light absorbed in the sample. With the O-ring in place, leakage is reduced to less than the noise level at 20 cm^{-1} .

A superconducting solenoid wound around the sample chamber can be used to drive samples of Pb, In, or Nb normal. However, the magnetic field usually brings about a reduction in signal of a factor of five and an increase in noise from the detector. This reduction is attributed to the increase

in heat capacity and thermal conductivity of the superconducting O-ring and solder when they too are driven normal. The reduction is less severe when copper is used as an O-ring material. The high T_C samples can not of course be driven normal so background spectra are provided by separate runs on brass foils.

5. Sample preparation

The samples used in the reflectivity experiments were rolled foils of pure lead and lead-indium alloy, evaporated films of pure lead and bulk samples of mercury. The foils were annealed just below the melting point for 48 hours under a hydrogen atmosphere and etched in a mixture of 75% glacial acetic acid and 25% hydrogen peroxide. The films were evaporated in a vacuum of 10^{-7} Torr to a thickness of 30μ at a deposition rate of about $10\mu/\text{min}$. 4.2 K resistances for the films, lead foils and lead-indium foils were 0.1, 0.03 and $0.45 \Omega \text{ cm}$ respectively. The mercury samples were formed by placing a pool of mercury in a stainless steel dish in the bottom of a cavity at room temperature, evacuating the cavity and cooling with liquid nitrogen without annealing.

For direct absorption measurements films of lead and of indium were evaporated, under the same conditions as above, onto substrates of 0.002 in. brass foil. The niobium samples consisted of films evaporated onto 0.02 in. copper foils, held at 500°C , in a vacuum of 10^{-9} Torr. The Nb_3Sn samples were RCA vapour deposited magnet ribbon.

CHAPTER IV

RESULTS

1. Lead Foil

The results of reflectivity measurements on a pure lead foil are shown in figure (6). The quantity plotted is the first derivative of the experimental spectrum given by equation (50).

$$(51) \quad S'(\omega) = \frac{d}{d\omega} (A_S(\omega) - A_N(\omega))$$

Within the simple theory, the phonon contribution to S' is given by the derivatives of Equations (47) and (48)

$$(52) \quad \frac{d}{d\omega} A_S(\omega) = \frac{4\pi^2\Delta}{\omega\omega_p} \phi_S(\omega) \alpha_{tr}^2 F(\omega-2\Delta)$$

$$\frac{4\pi\phi_S(\omega)}{\omega^2\omega_p} \int_0^{\omega-2\Delta} d\Omega \alpha_{tr}^2 F(\Omega) \left\{ \Omega E(k) + \omega \frac{(1-k^2)}{k^2} [E(k) - K(k)] \right\}$$

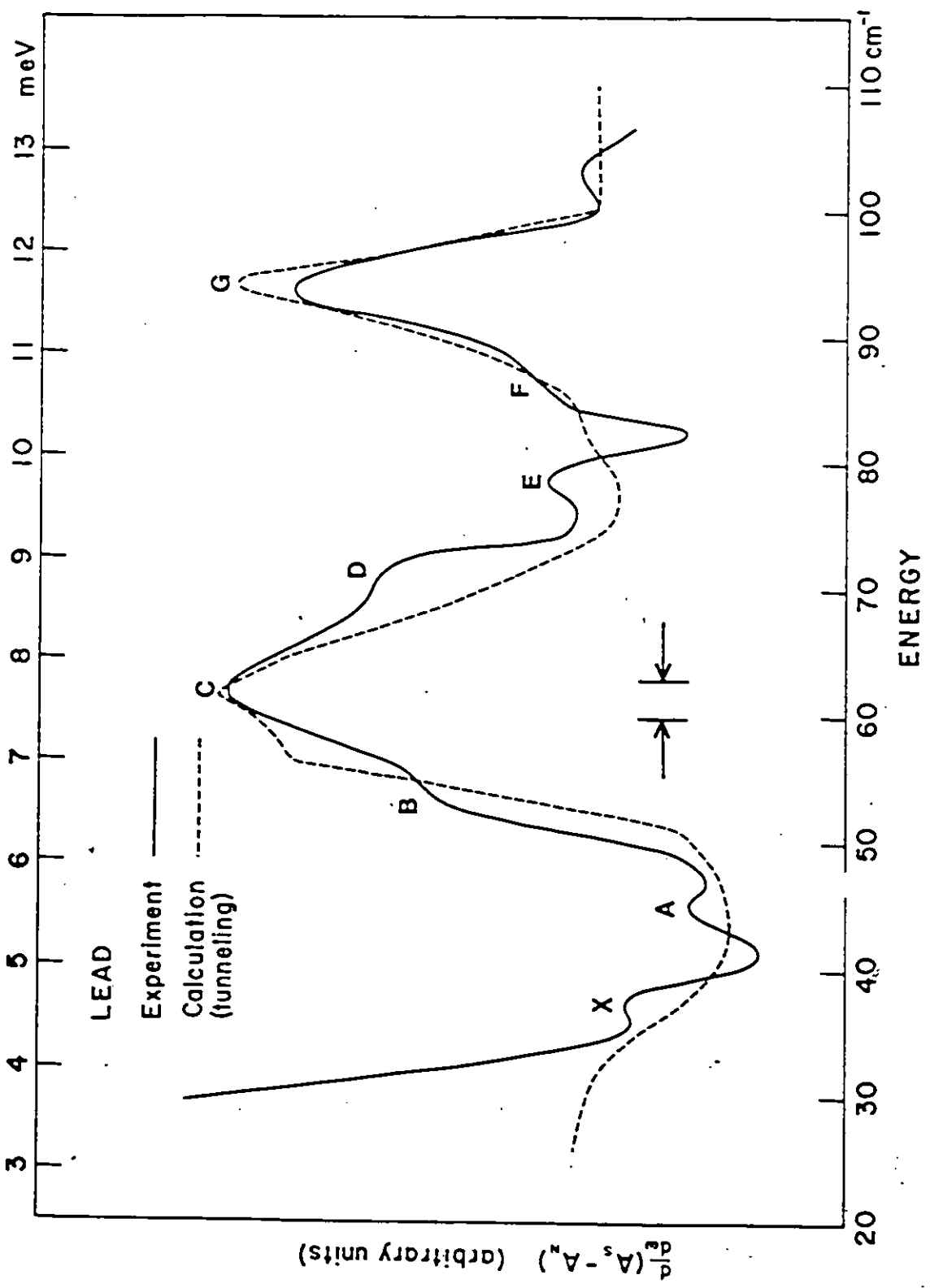
$$(53) \quad \frac{d}{d\omega} A_N(\omega) = \frac{4\pi}{\omega^2\omega_p} \phi_N(\omega) \int_0^{\omega} \alpha_{tr}^2 F(\Omega) d\Omega$$

where $k^2 = 1 - (2\Delta/(\omega - \Omega))^2$ and the quantities $\phi_S(\omega)$ and $\phi_N(\omega)$ which are expected to be slowly varying are assumed to be constant.

A calculation of the expected phonon structure has been made using the phonon spectrum $\alpha_0^2 F(\omega)$ derived from

FIGURE 6

Reflectivity results for a lead foil (isotropic) peaks in $\frac{d}{d\omega} (A_S - A_N)$ correspond directly to peaks in the phonon density of states. The calculation is based on Allen's theory and the density of states from tunneling measurements. The calculated curve has been displaced to higher frequency (by 5.5 cm^{-1}) so that the positions of peaks C and G agree. Peaks A, B, D, E and F are attributed to phonon structure that the tunneling measurements have missed. The rise in the experimental curve below 40 cm^{-1} is due to the energy gap ($2\Delta = 21.5 \text{ cm}^{-1}$). The origin of peak X is unknown.



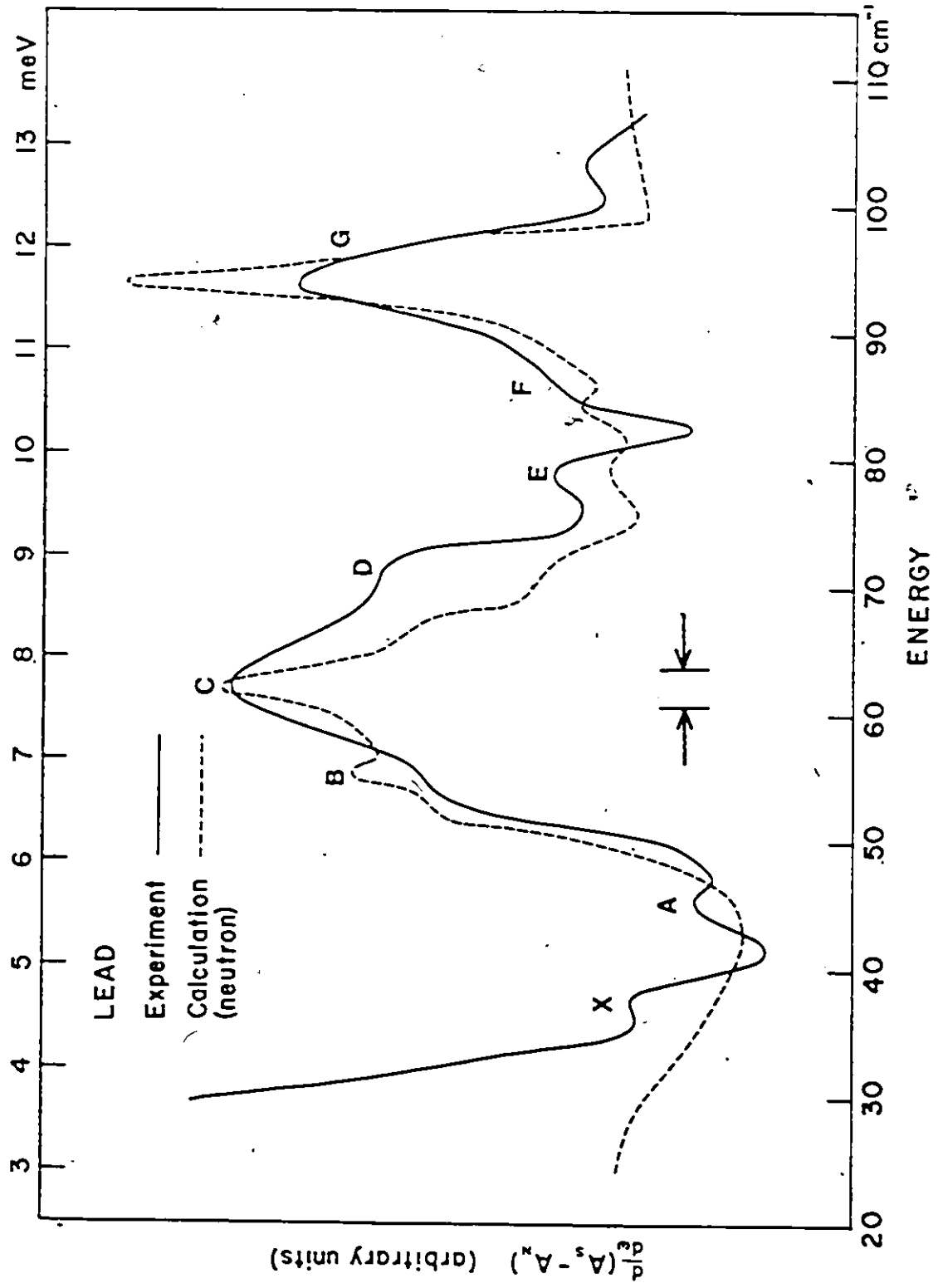
tunneling experiments (McMillan and Rowell 1969) in place of $\alpha_{tr}^2 F(\omega)$ in equations (52) and (53). The calculated curve plotted in figure (6) has been displaced to higher energy by 5.5 cm^{-1} (0.68 meV) so that the positions of the two main transverse and longitudinal peaks (c and G) agree with the experiment. In other words, the phonon structure is observed experimentally at higher energy than predicted by the simple theory. Apart from this shift, the overall shape of the spectrum is predicted quite well by the calculation. The rise in the experimental results below 40 cm^{-1} is due to the surface contribution to the absorption, which is not taken into account in the calculation.

Apart from the two main peaks, however, the experiment shows considerable fine structure not predicted by the calculation (peaks X, A, B, D, E, F). In equations (52) and (53) the integrals over $\alpha^2 F$ smooth out any structure in the phonon spectrum, so any sharp peaks in the experiment can be identified with corresponding peaks in the phonon spectrum through the direct term, $\alpha^2 F(\omega - 2\Delta)$ in equation (52). Thus, peaks A, B, D, E and F appear to arise from structure in $\alpha^2 F$ that the tunneling measurements have missed. Peak X is probably too low in frequency to be attributed directly to phonons.

In figure (7) the same experimental results are compared with a calculation based on the density of states derived from inelastic neutron scattering. The calculated curve has again been shifted to higher frequency, this time

FIGURE 7

The same data as in figure 6 compared to a calculation based on the density of states derived from neutron scattering. The calculation has again been shifted to higher frequency (by 4.5 cm^{-1}). Peaks B, D, E and F are predicted by the calculation.



by 4.5 cm^{-1} (0.56 meV). Here all the phonon fine structure except peak A can be identified with similar structure in the neutron derived density of states.

Since there is good agreement in general spectral shape between 40 and 100 cm^{-1} it is possible to use the simple theory to extract a phonon density of states from the experimental data. The theoretical expression for the phonon contribution is of the form

$$(54) \quad S'(\omega) = g_1(\omega) \alpha_{\text{tr}}^2 F(\omega - 2\Delta) + \int g_2(\omega, \Omega) \alpha_{\text{tr}}^2 F(\Omega) d\Omega$$

If the experimental data are put in for $S'(\omega)$ then equation (54) is an integral equation for $\alpha_{\text{tr}}^2 F(\omega)$ whose numerical solution is straightforward. Additional input into the inversion routine is a value for the energy gap ($2\Delta = 21.5 \text{ cm}^{-1} = 2.67 \text{ meV}$), which is determined experimentally from the onset of the surface absorption, and a value for the upper frequency cutoff of the phonon spectrum, which is apparent in the data and in good agreement with tunneling and neutron data. The contribution of the surface absorption is roughly taken into account by adding an adjustable constant to the RHS of equation (54). $\phi_S(\omega)$ and $\phi_N(\omega)$ are taken to be constant and equal. The final result depends only weakly on the ratio ϕ_S/ϕ_N .

Since the theory and experiment only agree above 40 cm^{-1} an assumption must be made about the phonon spectrum below 19 cm^{-1} ($40 \text{ cm}^{-1} - 2\Delta$). It is expected that $\alpha_{\text{tr}}^2 F$ should go to 0 as ω^2 at low frequency (Carbotte 1975) and this is assumed in the calculation.

The results of the inversion of the data in figure (6) are shown in figure (8), compared to the tunneling derived $\alpha_0^2 F(\omega)$, and in figure (9), compared to the neutron derived $F(\omega)$. The far infrared has been shifted down in frequency so that the positions of the main transverse and longitudinal peaks agree. The major discrepancies between far infrared and tunneling and far infrared and neutron are the frequency shift and the width of the main transverse peak.

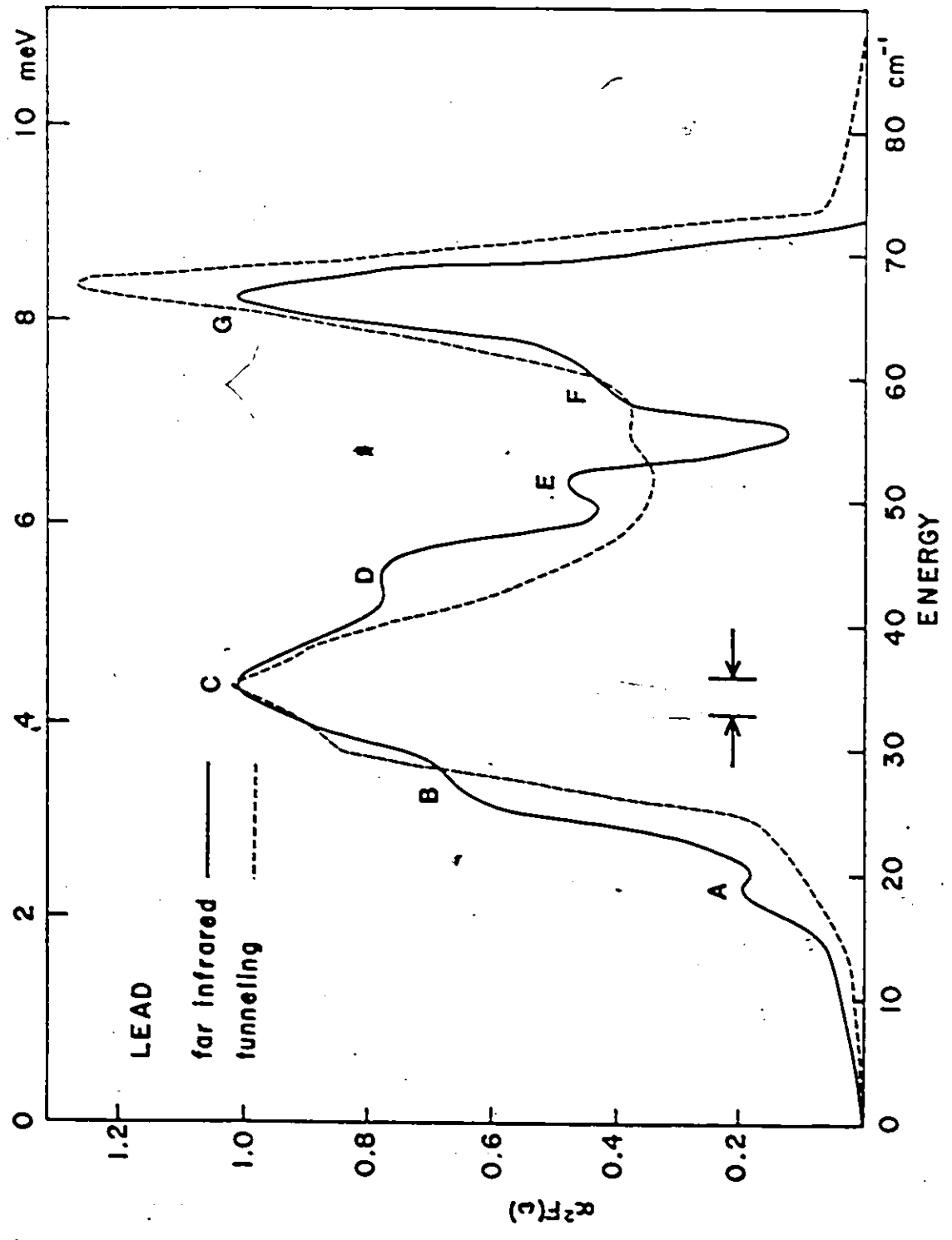
The extra width of the transverse peak cannot be entirely attributed to the low experimental resolution but may well be due to the inadequacies of the simple theory. Most of the shift is certainly due to the theory but there is a 1 cm^{-1} discrepancy between the neutron and tunneling results themselves.

There is also a difference in the height of the longitudinal peak G. This again could be an artifact of the simple theory or it could be due to the difference between $\alpha_{\text{tr}}^2 F(\omega)$ and $\alpha_0^2 F(\omega)$. Allen (1970) has calculated that the longitudinal peak should be half as high in $\alpha_{\text{tr}}^2 F(\omega)$ as in $\alpha_0^2 F(\omega)$. This is clearly an overestimate of the difference. Calculations by Tomlinson and Carbotte (1974) give $\alpha_{\text{tr}}^2 / \alpha_0^2 = 0.90$ at the longitudinal peak which is in better agreement with the value of 0.80 obtained here.

Of more significance is the appearance in the far infrared data of fine structure which is missing in the tunneling results. Peaks B, D, E and, to a lesser extent, F, agree well with structure in the neutron derived $F(\omega)$. A

FIGURE 8

The phonon density of states of lead derived from the reflectivity measurements compared to that derived from tunneling. The transverse peak in the far infrared data is broader than in the tunneling, probably as a result of the inadequacies of the simple theory. The tunneling density of states contains none of the fine structure seen in the far infrared. The infrared data has been shifted down in energy by 5.5 cm^{-1} .



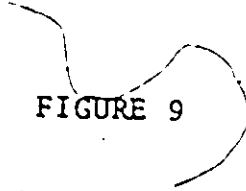
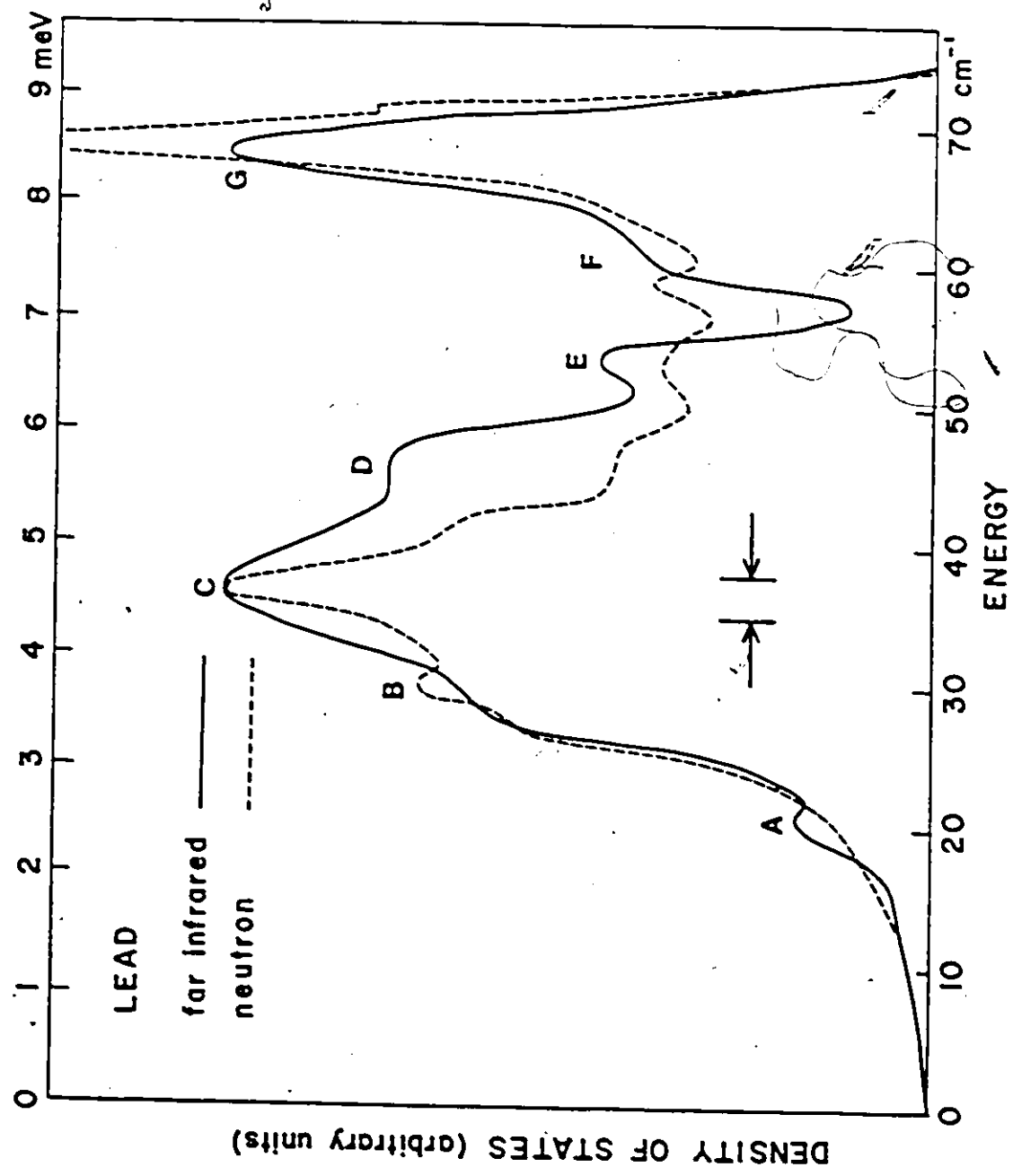


FIGURE 9

The phonon density of states of lead derived from the reflectivity measurements compared to that derived from neutron scattering. Most of the fine structure seen in the far infrared agrees with that in the neutron results. Peak A is attributed to phonon lifetime effects associated with the superconducting energy gap. The far infrared data have been shifted down in energy by 4.5 cm^{-1} .



more recent calculation of $\alpha_0^2 F$ by Coulthard (1973), based on the tunneling experiments of Blackford and March (1968, 1969), also shows peak B, but otherwise agrees with McMillan and Rowell.

Peak A, which is not present in either the tunneling or the neutron results, is due to phonons of energy close to the superconducting gap energy 2Δ , and can be attributed to phonon lifetime effects associated with the superconducting transition. This peak is not expected in the neutron measurements as they were performed above the transition temperature. The lifetime of phonons with energy less than 2Δ is very long (Dynes and Narayanamurti 1972) since these phonons have insufficient energy to create excitations of the superconducting electrons. Above 2Δ loss of energy to the electrons becomes possible and there is an abrupt change in the phonon lifetime. This discontinuity in the imaginary part of the phonon self-energy leads to a change in the real part and a corresponding discontinuity in the phonon density of states. A rough calculation of this effect by Schuster (1973) predicts a net downward shift in phonon energies when the metal goes superconducting and a singularity in the density of states at 2Δ . Thus, the observed peak at 20.5 cm^{-1} (figure 9), compared to $2\Delta = 21.5 \text{ cm}^{-1}$, is in good agreement with the theory.

For an impure metal the phonon lifetime below 2Δ is limited by impurity scattering and the discontinuity at 2Δ is less severe. Figure (10) shows experimental results for an alloy of lead with 0.5 at.% indium. Here the peak at A has


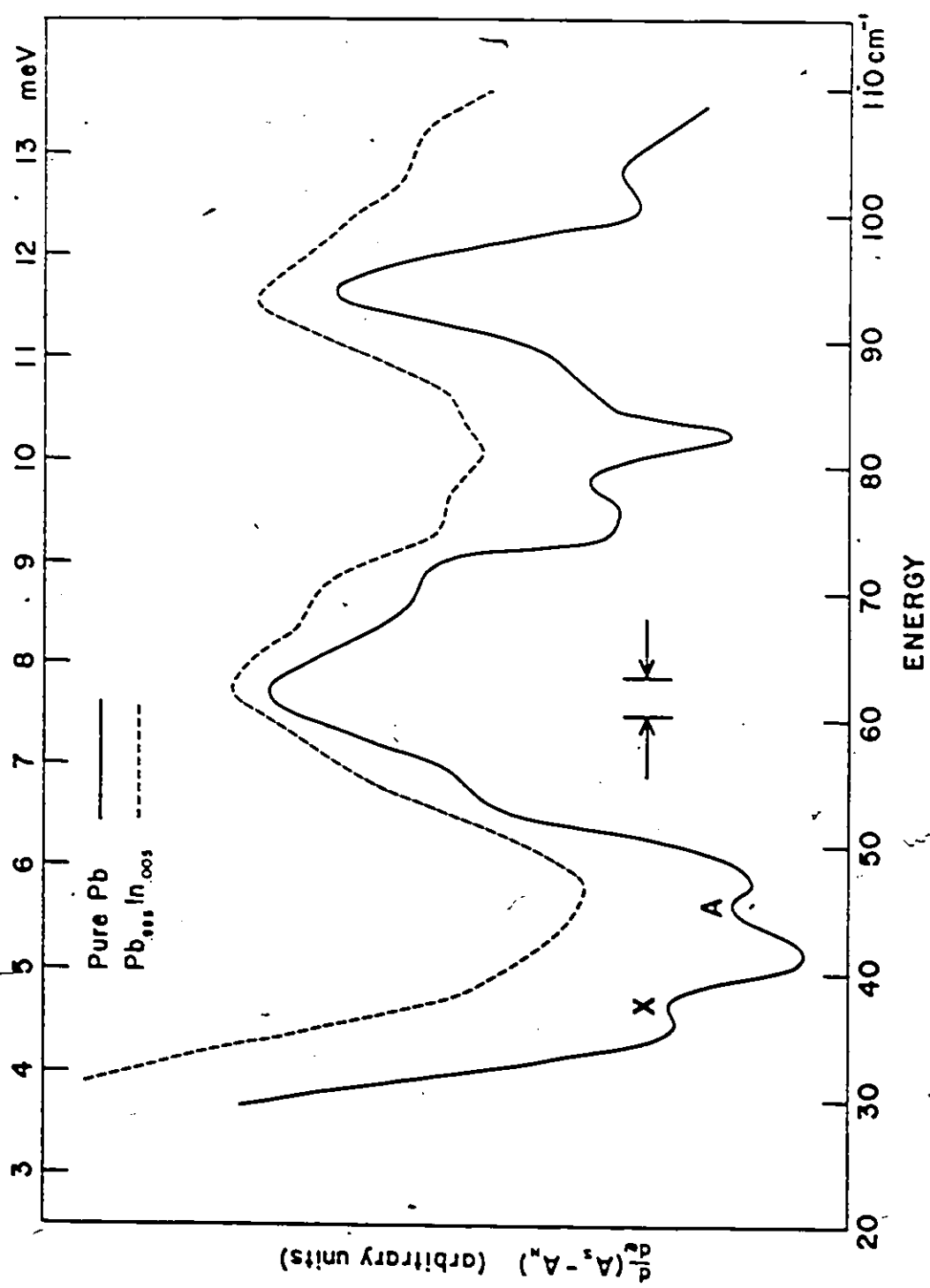


FIGURE 10

Reflectivity measurements on a dilute lead-indium alloy. All of the phonon structure is weaker in the alloy but peak A disappears completely. Peak X also disappears.



disappeared while the rest of the phonon structure remains essentially unchanged, although it is somewhat broadened. The peak at X has also disappeared.

From the area under peak A, about 1% of the area of the total transverse peak, it is possible to estimate the lifetime of phonons in the neighbourhood of 2Δ . It is found that these phonons have a width $\Delta\omega$ of about 12% of their energy. This estimate is necessarily crude since the theory is for longitudinal rather than transverse phonons and a BCS superconductor and the experiment is not fully resolving the peak, but the answer is consistent with the measurements of Axe and Shirane (1973) on Nb. The results for Nb give a width of 5% but the electron-phonon coupling is weaker in Nb by about a factor of two.

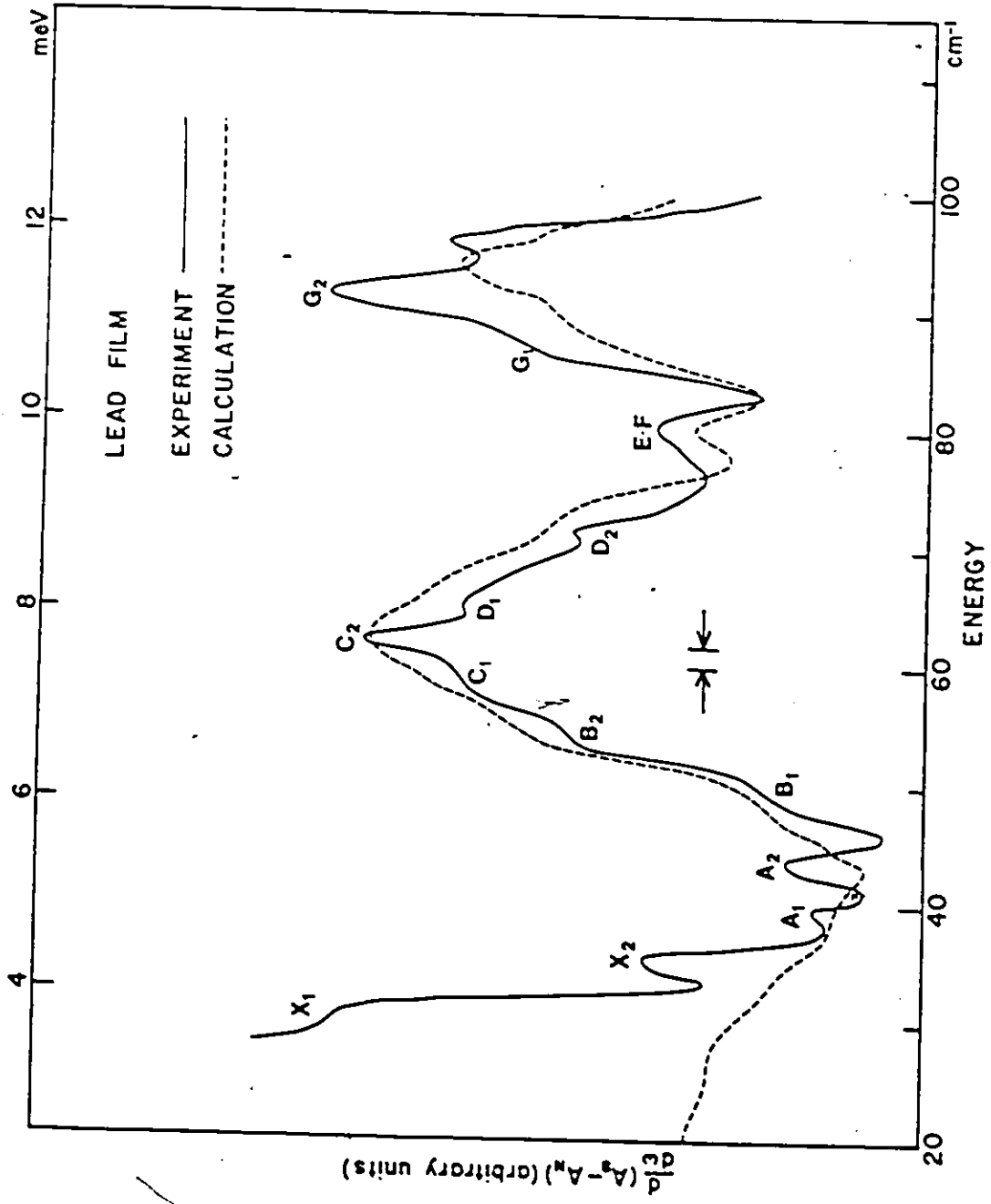
2. Lead Film

Figure (11) shows results for an evaporated film of pure lead. Here all the phonon fine structure present in the foil results appear to be split. This is interpreted in terms of the double energy gap in an anisotropic sample of lead. The two energy gaps arise from the splitting of the Fermi into a hole surface in the 2nd Brillouin zone and an electron surface in the 3rd zone (Anderson and Gold 1965), the energy gap being different on the two surfaces.

The gaps on the electron and hole surfaces are denoted $2\Delta_1$ and $2\Delta_2$, respectively. In figure (11) the phonon peaks have been labelled by a letter indicating the corresponding peak in the foil results and a subscript denoting the

FIGURE 11

Reflectivity results for a lead film (anisotropic). All of the structure seen in the foil results is split due to the double gap in an anisotropic sample of lead. The calculation is based on a splitting in 2Δ of 5 cm^{-1} and the phonon density of states derived from the foil measurements. All of the phonon structure seen in the experiment is predicted by the calculation but weakly. It is concluded that the phonon structure is sharper than is indicated by the foil results. Peak X is also split.



appropriate gap. The dashed line is a calculation of the expected spectrum using the density of states derived from the foil measurements and adding together contributions from the two gaps.

$$(55) \quad S'_{\text{TOTAL}}(\omega) = S'(\omega; \Delta_1) + S'(\omega; \Delta_2)$$

All the phonon structure visible in the experiment is reproduced by the calculation, although weakly. Peaks A, B, C, D, and G appear split while peaks E and F combine to produce the small peak at 80 cm^{-1} . The value of the larger gap, $2\Delta_2 = 22 \text{ cm}^{-1}$ (2.73 meV), is accurately determined by the position of peak C₂. Best overall agreement between the experiment and calculation is obtained with $2\Delta_1 = 17 \text{ cm}^{-1}$ (2.11 meV). The absorption edge at the gap shows weak structure consistent with this figure. However, this value for $2\Delta_1$ gives a splitting ($2\Delta_2 - 2\Delta_1$) of 5 cm^{-1} (0.62 meV) which is somewhat higher than the maximum value of 3.5 cm^{-1} (0.43 meV) observed in the tunneling measurements of Blackford and March (1969). Also peak A only seems to be split by 3.5 cm^{-1} . Thus the value for $2\Delta_1$ is somewhat uncertain. Peaks A₁ and A₂ appear at a slightly lower energy than predicted by the calculation and correspond to a peak in the phonon density of states at 19 cm^{-1} rather than 20.5 cm^{-1} as in the foil results. Since the position of peak A is determined by the effect of the energy gap on the phonons the downward shift is to be expected as the average gap in the double gap system is lower than the single gap in the isotropic case. The results would suggest an average gap of 20 cm^{-1} (2.48 meV) which seems reasonable.

The results for this sample can therefore be explained reasonably well on the basis of contributions to the absorptivity for the two energy gaps, but the observed structure is much sharper than that predicted on the basis of the density of states derived from measurements on the isotropic foil, in which only a single gap is apparent. This would suggest that the structure in the density of states is in fact not being fully resolved in the foil measurements, and that, in particular, B and D are in fact pronounced peaks rather than shoulders on the sides of the main transverse peak. In the case of B this is consistent with the neutron data and Coulthard's calculations of the tunneling density of states.

Peak X appears split in the film measurements (30 and 35 cm^{-1}) and at a lower energy than in the foil (37 cm^{-1}) in the same way as peak A. This would indicate that it is in some way associated with the energy gap but its origin is not obvious.

3. Comparison with Strong Coupling Theory

The simple theory discussed so far has two major drawbacks. Firstly, the anomalous skin effect has been ignored and, secondly, the superconductor has been treated by BCS theory. Neglecting the non-local nature of the electric field is expected only to introduce errors that are smooth functions of frequency and so have little effect on the derivatives of the absorption. However, strong coupling

corrections to the theory of superconductivity can be expected to give additional structure due to the influence of the phonon spectrum on the electron self-energy. The second drawback is therefore more serious.

Both the limitations have been overcome in the calculation by Swihart and Shaw. Unfortunately the calculation was not carried out in sufficient detail to permit a comparison with the experimental derivative $S'(\omega)$. A comparison is possible only for the undifferentiated data, which is a far less sensitive test. This is shown in figure (12).

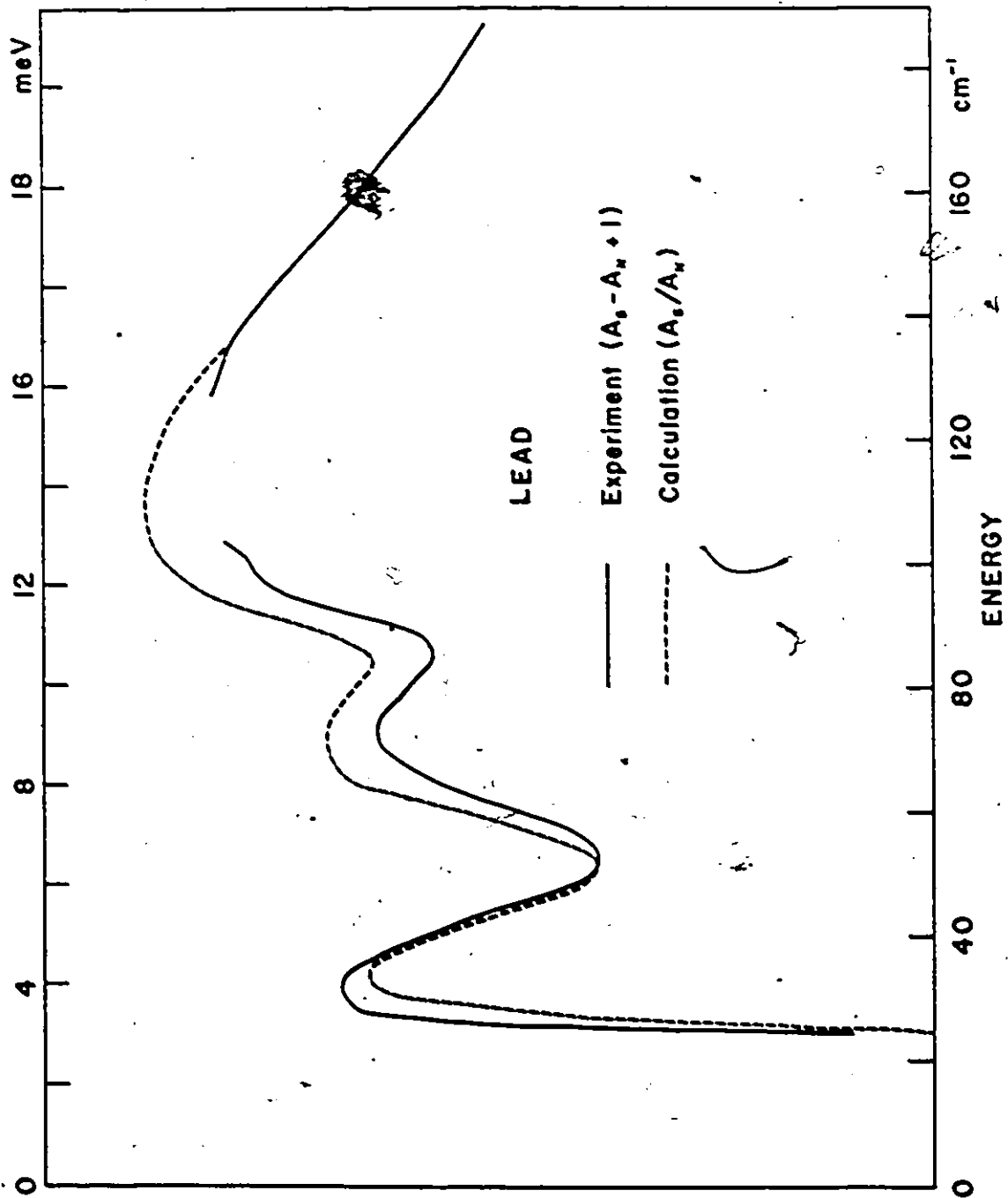
The experimental curve is $S(\omega) = 1 + n(A_S - A_N)$ for a pure lead film. The calculated spectrum is the ratio A_S/A_N . These are, of course, different, but have the same general behaviour except near the gap frequency. At high frequencies both quantities approach 1 and the phonon structure, coming primarily from A_S , is the same in both. Below the gap $S(\omega)$ goes to $1 - A_N(\omega)$, whereas the ratio goes to zero, so the two quantities diverge; but the ratio is the only curve currently available for comparison to the experiment.

Bearing in mind that the two quantities are different, it can be seen that the calculation agrees well with the experiment throughout the region 25 to 190 cm^{-1} , although no reliable experimental data are available between 105 and 125 cm^{-1} . The calculation shown here is for the case of diffuse electron scattering at the metal surface. The case of specular reflection gives results that are similar but with stronger phonon structure and in poorer agreement with the experiment.



FIGURE 12

Results for a lead film (not differentiated) compared to the full strong coupling calculation of Swihart and Shaw. The measured and calculated quantities are different but have the same general behaviour. \leftarrow A 1 cm^{-1} discrepancy is noted in the position of the phonon peaks but otherwise the agreement is good.



There is still a discrepancy in the position of the phonon peaks, but of only 1 cm^{-1} here, rather than 5 cm^{-1} as in the simple theory. This calculation is based on the tunneling data of Rowell and McMillan which give phonon peaks 1 cm^{-1} below those found by neutron scattering. Therefore, combination of the neutron measurements and these far infrared measurements would indicate that the frequencies measured by tunneling are too low by 1 cm^{-1} .

4. Indium

Direct absorption measurements were performed on indium evaporated onto a brass foil. A background was supplied by measurements of a polished brass foil performed the next day. The results are shown in figures (13) and (14) compared to calculations based on the neutron and tunneling densities of states (Rowell and Dynes 1971). These densities of states are shown in figure (15). The main factors visible in the experiments are a transverse mode (T_1) peaking at 65 cm^{-1} , a broader transverse mode (T_2) between 80 and 110 cm^{-1} ; and the longitudinal mode (L) at 135 cm^{-1} . A shoulder is apparent on the low frequency side of the T_1 peak at 50 cm^{-1} . These features are qualitatively reproduced by the calculation. Quantitatively, the agreement is poor though somewhat better for the neutron case than the tunneling case.

In order to obtain agreement in the frequencies of the transverse peaks the calculated curves have been shifted to higher frequency by 13 cm^{-1} (1.61 meV) but even

FIGURE 13

Direct absorption measurements on an indium film. The calculation, Allen's theory with the density of states from neutron scattering, predicts qualitatively the two transverse and the one longitudinal peaks as well as the shoulder on the low frequency side of the first transverse peak. The calculated curve has been shifted to higher frequency by 13 cm^{-1} . An additional shift of 5 cm^{-1} is needed for the longitudinal peak. Extra structure is seen at 20 and 160 cm^{-1} .

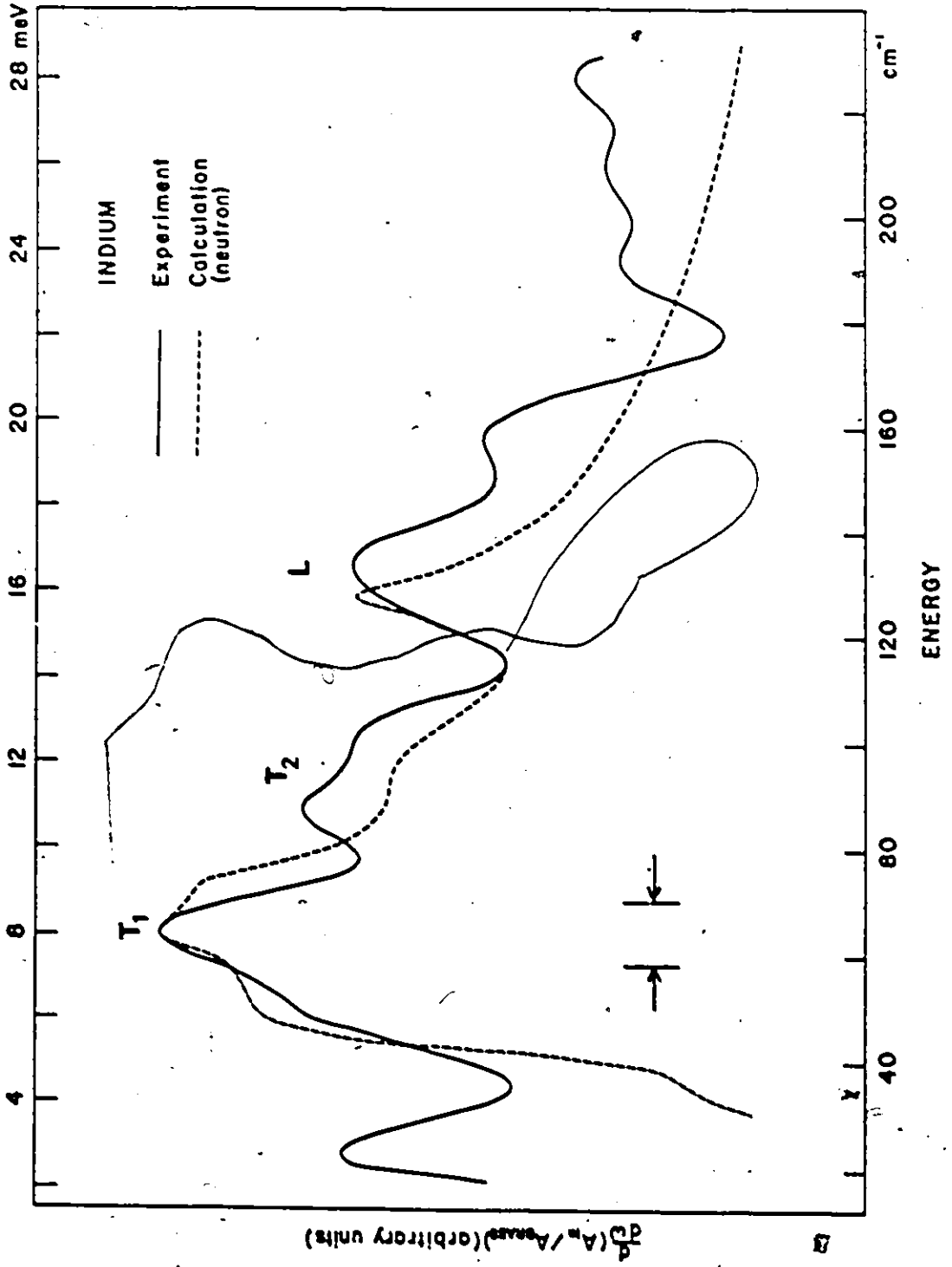


FIGURE 14

The same results for indium as in figure 13 compared to a calculation based on the tunneling derived density of states. The calculation has again been shifted by 13 cm^{-1} . The agreement is not as good here as when the neutron data are used.

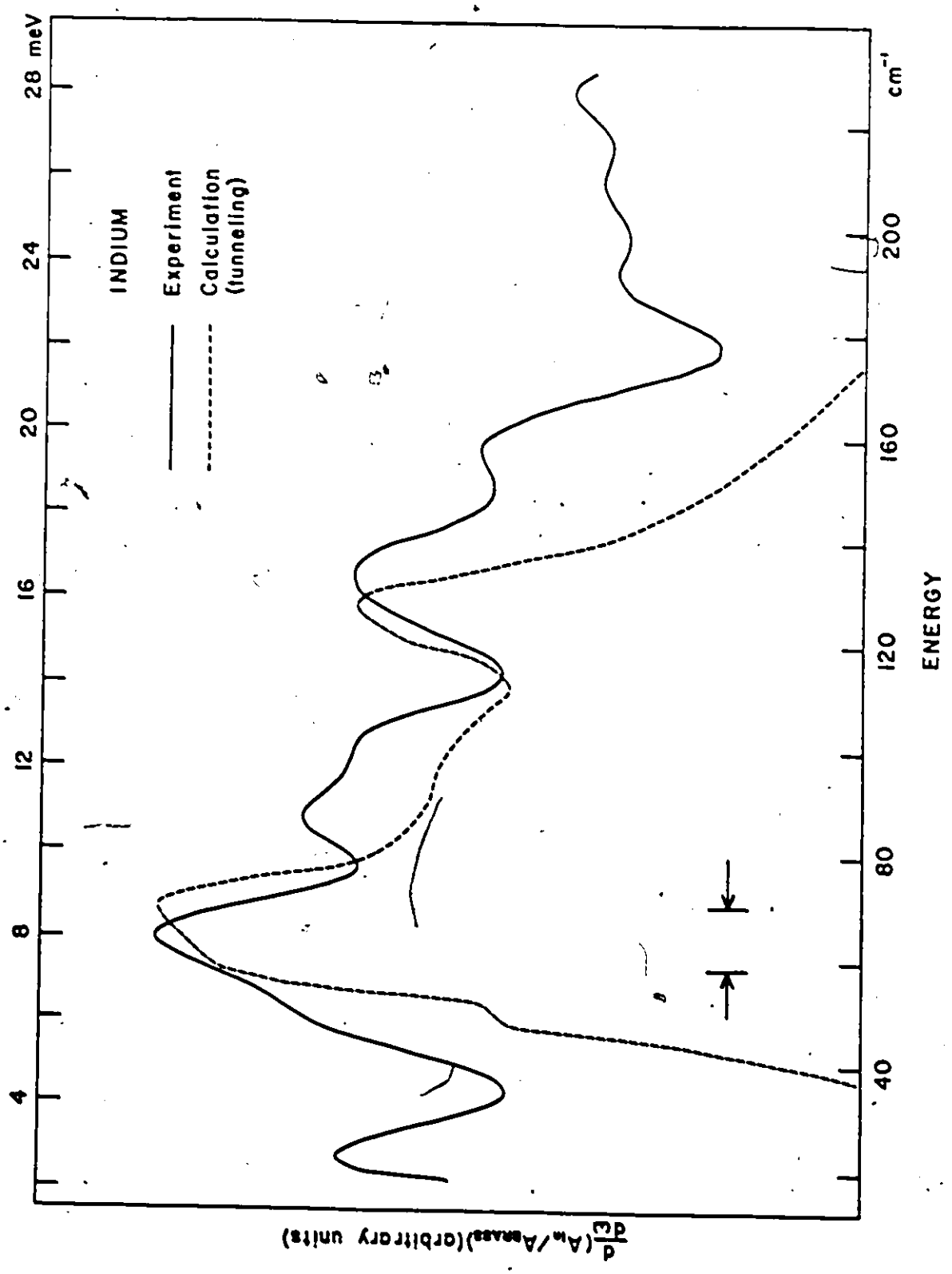
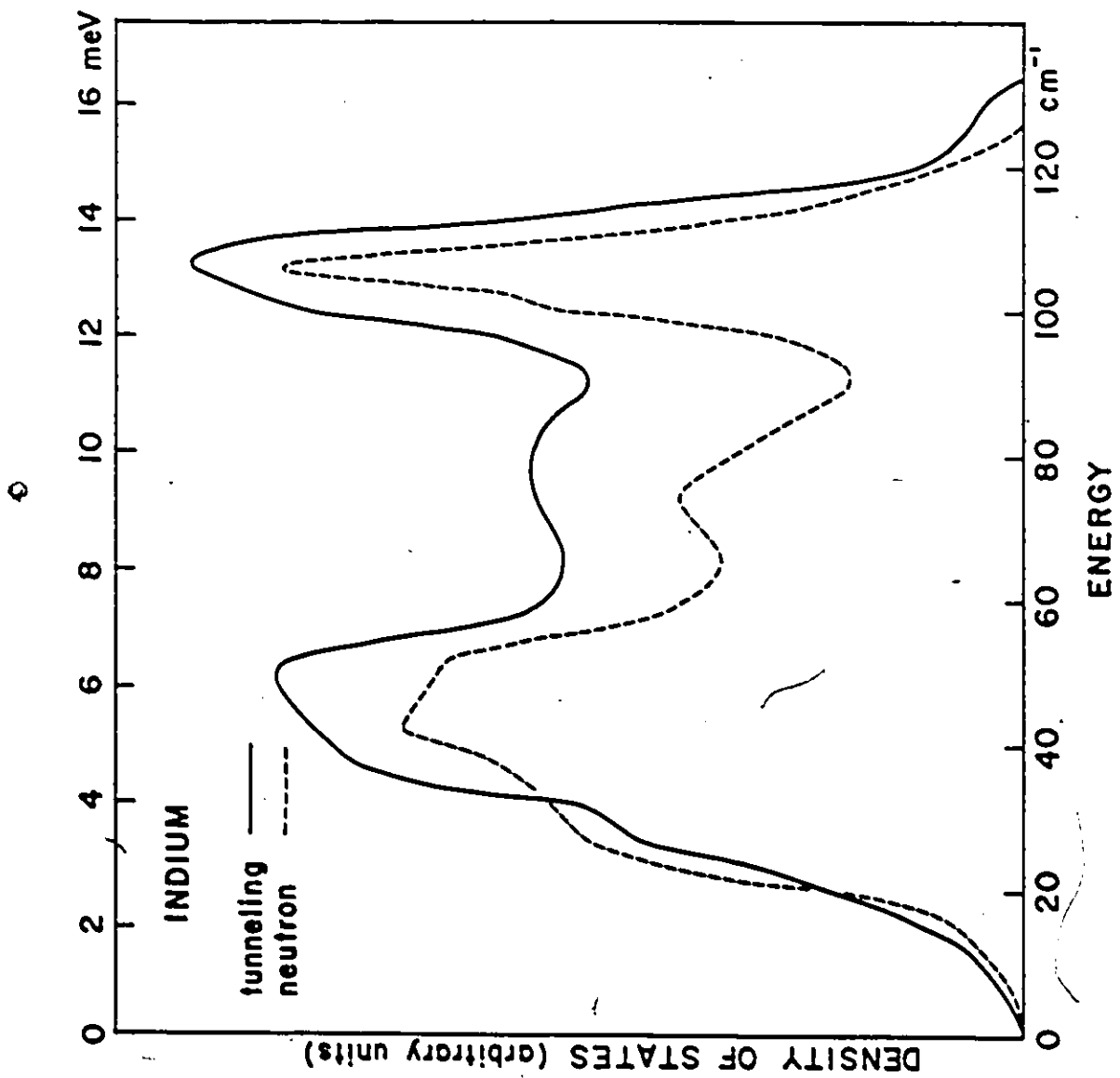


FIGURE 15

The phonon density of states of indium as
found by tunneling experiments and by neutron scattering.



this large shift is insufficient for the longitudinal peak. This large shift is surprising. Indium is a much weaker coupling material than lead so it would be expected that the simple theory would work much better in the case of indium. This discrepancy is discussed further in section 8. Additional structure in the experiment, not even qualitatively reproduced in the calculation, are peaks at 23 and 160 cm^{-1} . The apparent splitting of the T_2 peak is probably noise; the small ripples above 190 cm^{-1} certainly are. The peak at 23 cm^{-1} may well be the same feature as the mysterious peak X in lead; it is certainly too low in frequency to be attributed to a peak in the phonon density of states.

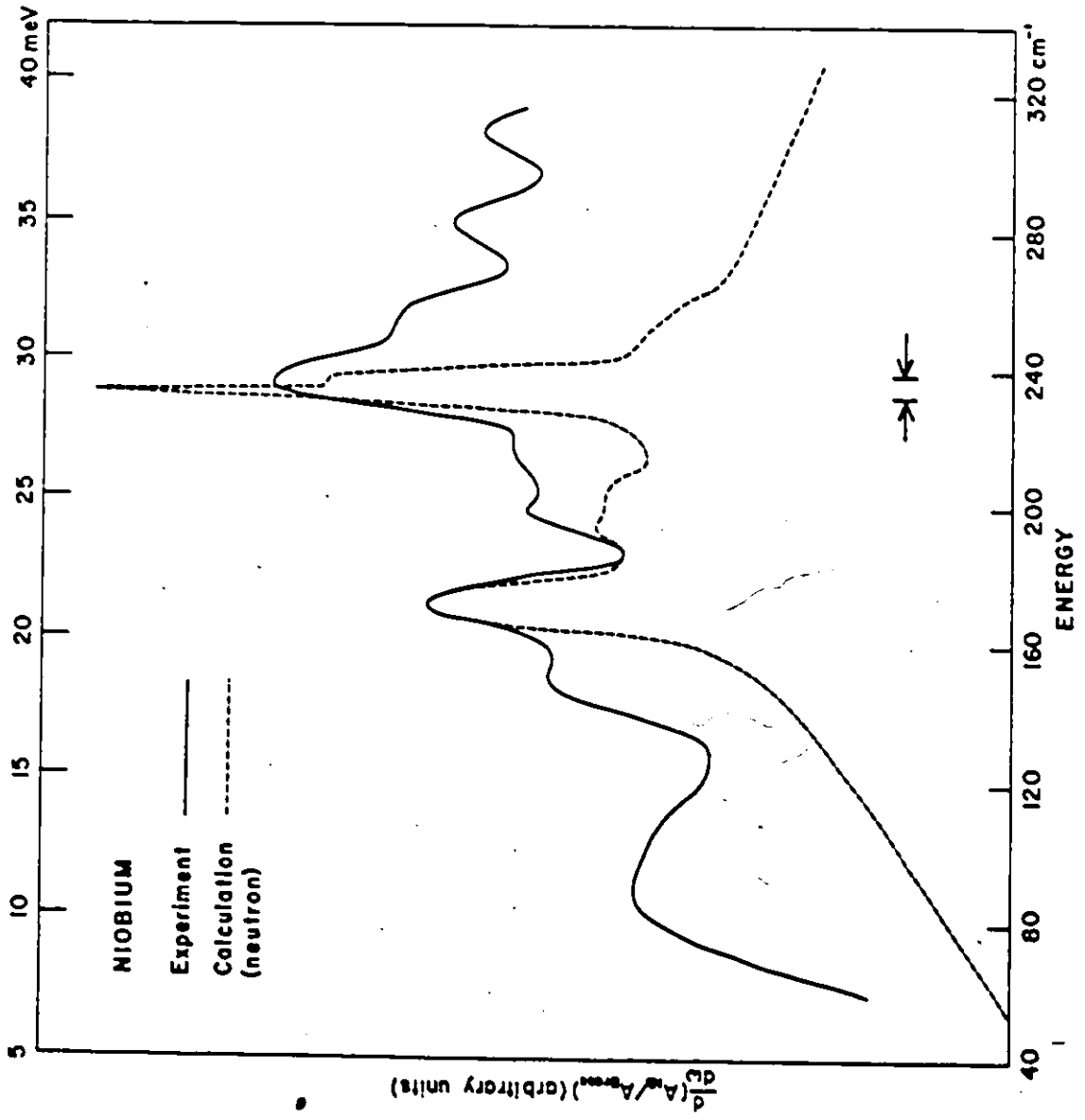
5. Niobium

Results for a niobium film on a copper substrate are shown in figure (16). The calculated curve is based on the neutron density of states (Nakagawa and Woods 1963). No tunneling density of states is available though phonon peaks have been observed in tunneling junction characteristics (Shen 1972a) in rough agreement with the neutron data.

There is considerable noise on this spectrum so it is not certain which of the smaller peaks are real but the main transverse and longitudinal peaks, at 172 and 236 cm^{-1} respectively, are clear. Here the calculation has been shifted to higher frequency by 23 cm^{-1} (2.85 meV). Again there is a peak, at 90 cm^{-1} , which is too low in energy to be caused directly by phonons.

FIGURE 16

Direct absorption measurements on a film of niobium. The high noise level makes the smaller structure uncertain but the main transverse and longitudinal peaks are clear. An additional broad peak is seen at 90 cm^{-1} . The calculation uses the neutron derived density of states and has been shifted to higher frequency by 23 cm^{-1} .



6. Mercury

Reflectivity measurements were performed on bulk samples of mercury by placing a pool of the liquid in a hemispherical cavity and then freezing. This technique provides only a small number of reflections off the sample so the absorption is weak. The results are shown in figure (17). The large peak at 14 cm^{-1} is due to the energy gap. The calculation, based on $\alpha_0^2 F$ calculated by McMillan and Rowell (1969) from experiments by Bermon and Ginsberg (1964), predicts the peak at 29 cm^{-1} with a shift of 1 cm^{-1} . The source of the slightly weaker peak at 21 cm^{-1} is again unclear.

7. Nb₃Sn

Absorption measurements were made on a commercial ribbon of Nb₃Sn vapour deposited on stainless steel. The results are shown in figure (18) compared to a calculation using the density of states found from tunneling by Shen (1972b). The peak at 40 cm^{-1} is due to the energy gap ($2\Delta = 36 \text{ cm}^{-1} = 4.47 \text{ meV}$) and the broad peak at 95 cm^{-1} can be identified with that seen in the tunneling data. There is no evidence of the peaks expected at about 160 and 230 cm^{-1} . Little can be concluded from these results since the surface of the sample is obviously of poor quality. As in Shen's tunneling experiments on this type of sample the energy gap is found to be considerably lower than the bulk value, although the transition temperature of the ribbon is high (17 K). This is

FIGURE 17

Reflectivity results for mercury. The large peak at 14 cm^{-1} is due to the energy gap. The peak at 29 cm^{-1} can be attributed to the peak in the phonon density of states. The calculation is based on tunneling data and has been shifted up in frequency by 1 cm^{-1} . The origin of the peak at 21 cm^{-1} is unclear.

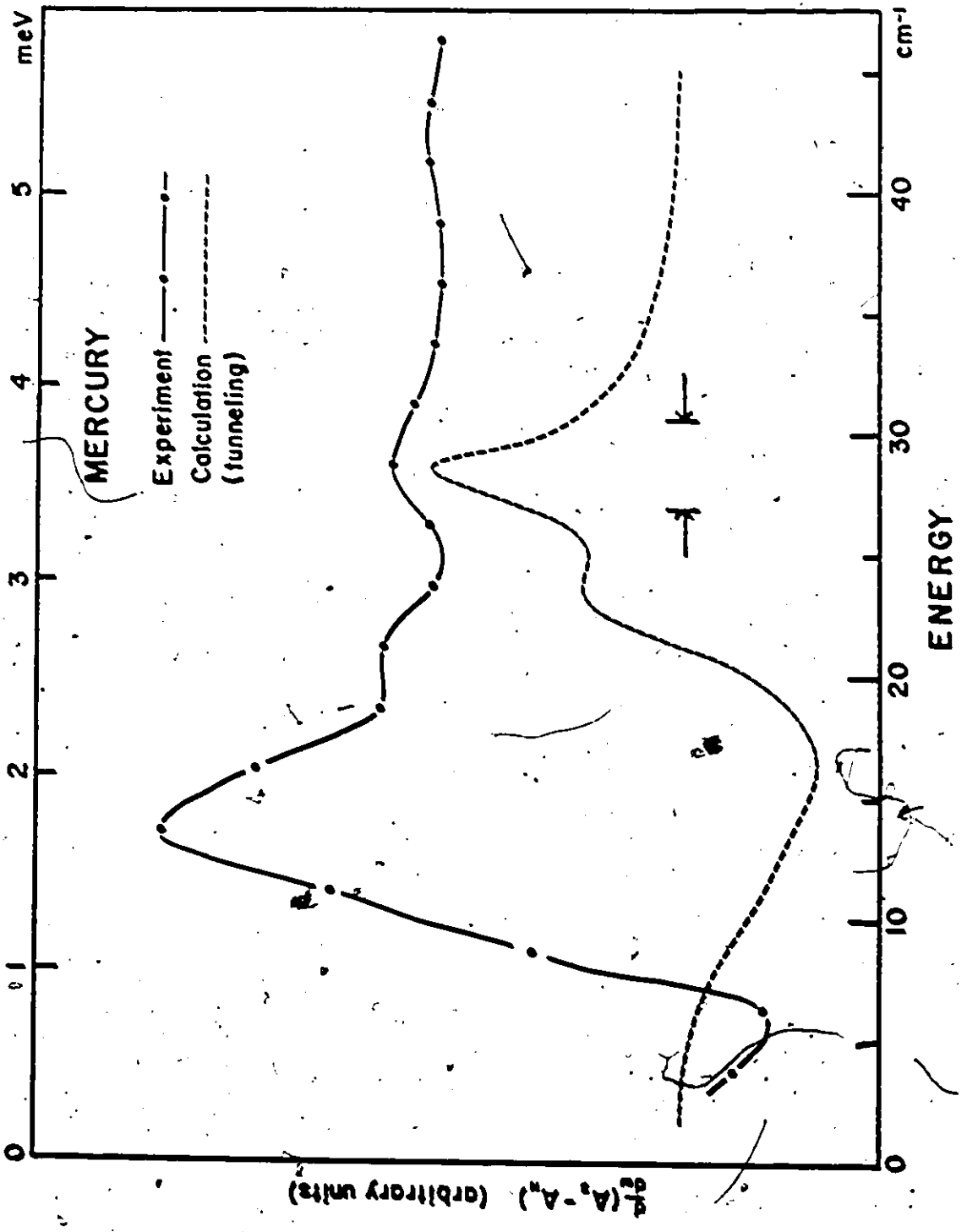
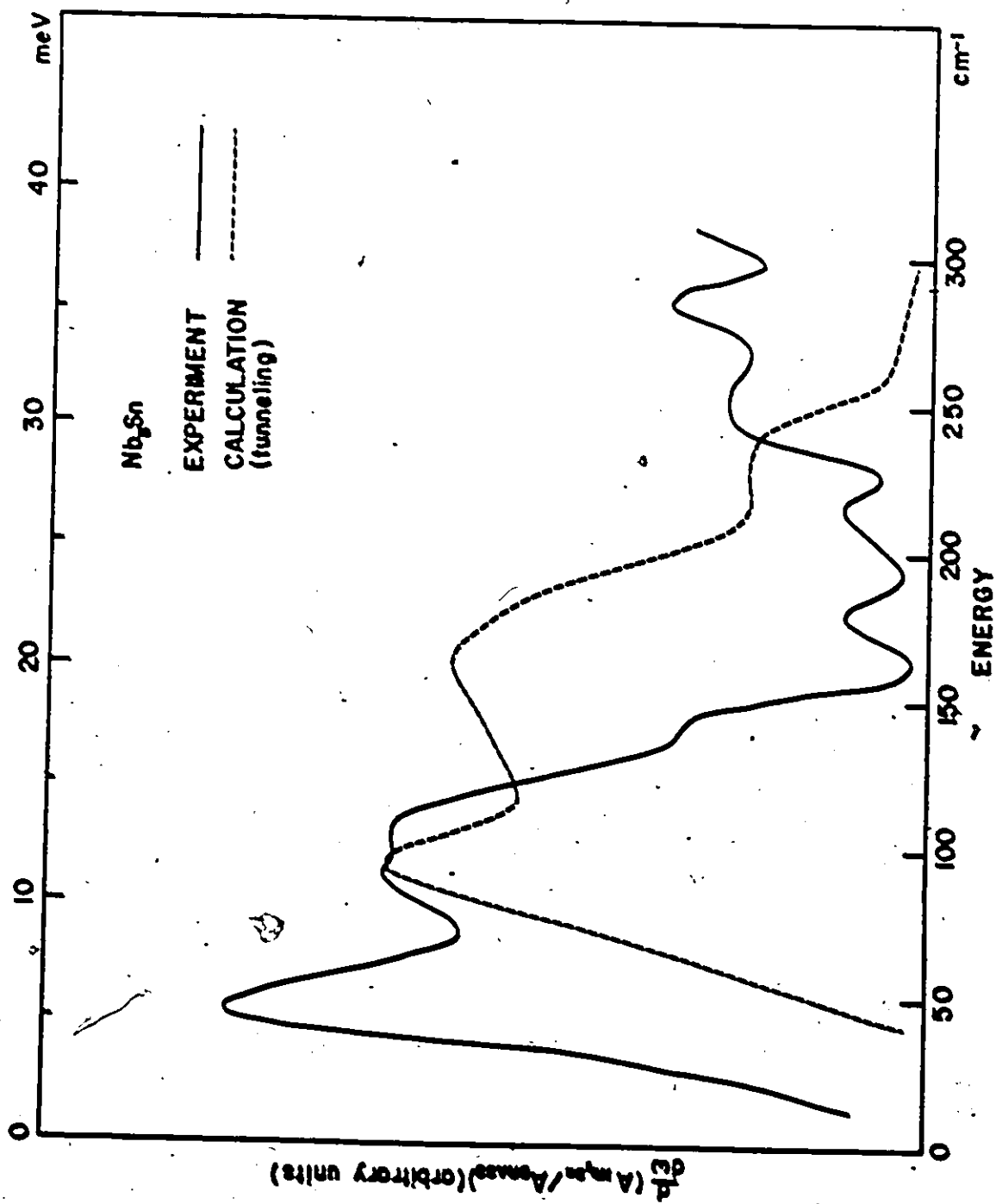


FIGURE 18

Direct absorption results for a commercial Nb_3Sn foil. The peak at 40 cm^{-1} is due to the energy gap. The calculation, based on tunneling data, predicts peaks at 100 , 170 and 240 cm^{-1} . Only the one at 100 cm^{-1} is observed.



taken as an indication of free niobium at the surface. Since the tunneling produced no phonon structure at all in these poor samples these results show considerable promise of significant measurements on Nb_3Sn when better samples become available.

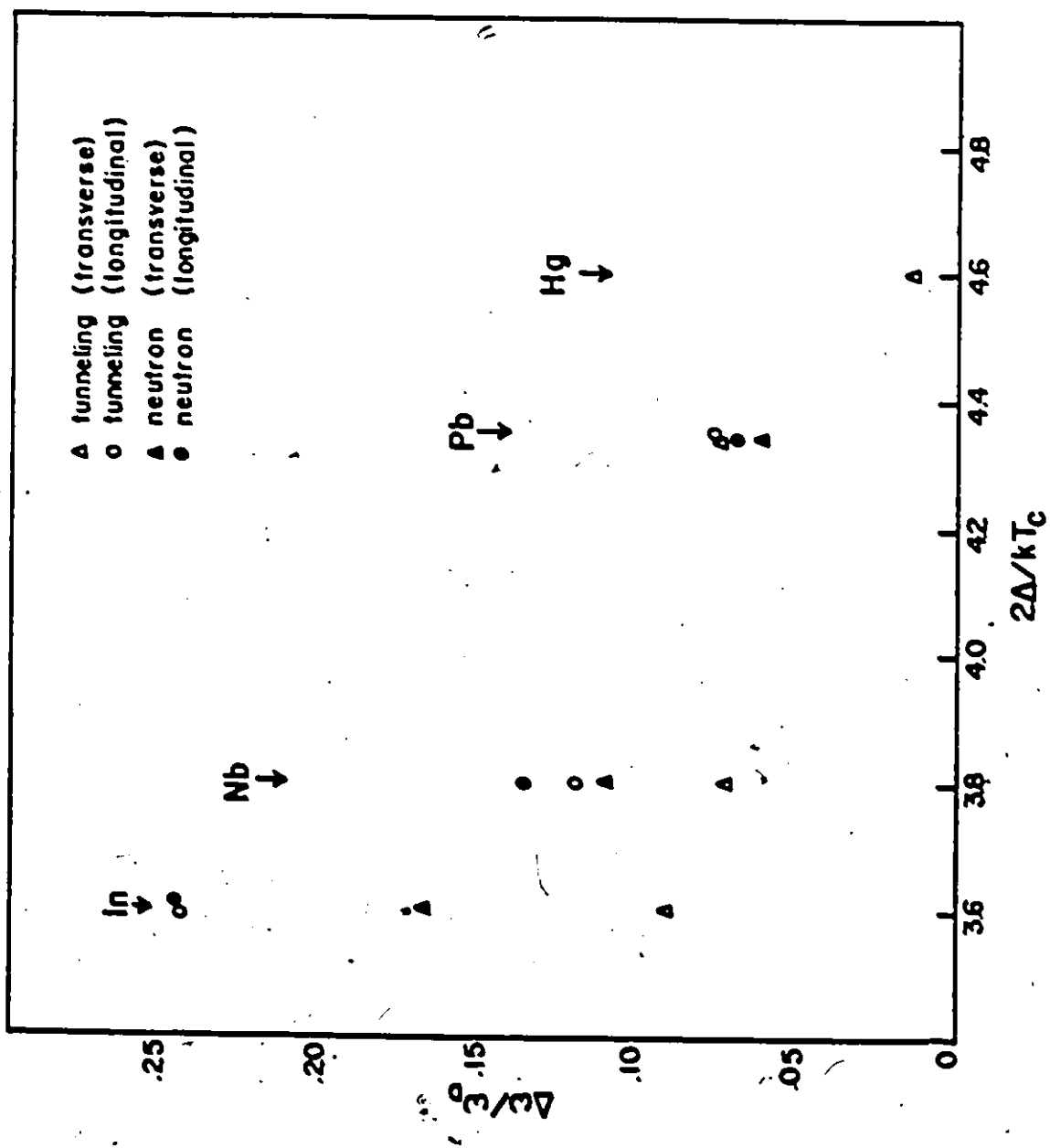
8. Breakdown of the Simple Theory

Allen's theory for the absorptivity gives results that are qualitatively correct but quantitatively poor. However, the errors involved are largely smooth functions of frequency so that the theory predicts quite well the derivative of the absorptivity, except for a shift in the observed phonon frequencies. Errors of this kind are not surprising in the case of a strong coupling material like lead but the simple theory was expected to be much better for weaker coupling materials.

Figure (19) shows a summary of the experimental results. The shift in observed frequency from that expected on the basis of tunneling and neutron data has been plotted versus the strong coupling parameter, $2\Delta/kT_c$. The frequency shift has been normalized to the Debye frequency. There is considerable scatter in the points, largely due to disagreement between tunneling and neutron data, but the general trend is clear. Contrary to expectation, the theory works best for the stronger coupling materials. That is, the frequency shift is smaller the more the parameter $2\Delta/kT$ departs from the BCS value of 3.5.

FIGURE 19

The difference between the observed positions of the phonon peaks and the positions expected on the basis of Allen's theory and phonon frequencies determined by tunneling and neutron scattering experiments is plotted versus the strong coupling parameter $2\Delta/kT_c$. The shift is normalized to the Debye frequency. The shift is smaller for the stronger coupling materials and so cannot be attributed solely to the assumption of BCS superconductivity. Much of the scatter is due to disagreement between the tunneling and neutron measurements.



The failure of the theory to give the correct frequencies cannot, therefore, be entirely attributed to the assumption of BCS superconductivity. It must, therefore, arise from the other weakness of the theory, the neglect of the non-local nature of the electric field. It is not easy to see how this comes about; but granted that the effect is there, it can be understood why it is worse in the case of the weaker coupling materials from the following.

The expression for the derivative of the absorption in the superconductor is (equation (52))

$$\frac{d}{d\omega} A_S(\omega) = \frac{4\pi^2\Delta}{\omega\omega_p} \alpha_{tr}^2 F(\omega-2\Delta) + \frac{4\pi}{\omega^2\omega_p} \int_0^{\omega-2\Delta} d\Omega \alpha_{tr}^2 F(\Omega) \left[\Omega E(k) + \frac{1-k^2}{k^2} (E(k) - K(k)) \right]$$

In the case of lead the first term is larger than the second by a factor of five or so and there is fairly good agreement with experiment. In weaker coupling materials the second term becomes more important and agreement with experiment deteriorates. This is to be expected since the second term is similar in form to the expression for the absorptivity (equation (47))

$$A_S(\omega) = \frac{4\pi}{\omega\omega_p} \int_0^{\omega-2\Delta} d\Omega (\omega-\Omega) \alpha_{tr}^2 F(\omega) E(k)$$

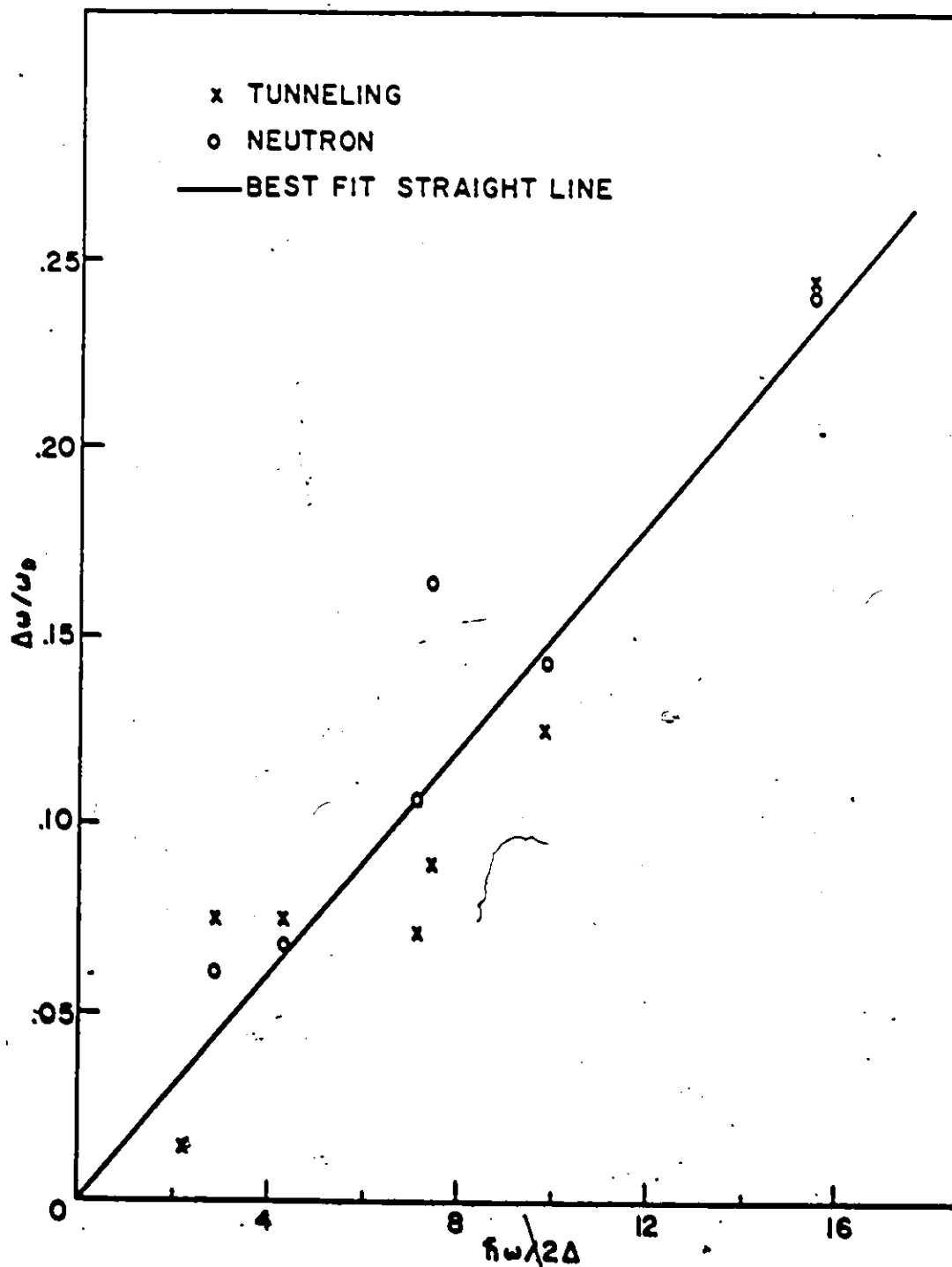
which does not agree with experiment very well (Allen 1970).

A measure of the relative strengths of the first and second terms is the ratio of their coefficients, $\frac{\omega}{\pi\Delta}$. The larger the ratio is the more important is the second term and the more severe is the expected error in the calculation of the derivative.

As a test of this argument the normalized frequency shift is plotted versus $\frac{\hbar\omega}{2\Delta}$ in figure (20). Again there is considerable scatter in the points but the general trend is in the expected direction. In fact, the points representing neutron results fall within 25% or so of a straight line. The line drawn is a least squares fit to all the data points.

FIGURE 20

The normalized frequency shift versus the reduced frequency $f\omega/2\Delta$. The trend is in the expected direction. The straight line is a least squares fit to the data points.



CHAPTER V

CONCLUSIONS

This work has demonstrated the applicability of far infrared absorption as a probe of the electron-phonon interaction in superconductors. The results are most complete for lead, the system most easily investigated experimentally and the only one for which calculations have been carried out taking into account both the anomalous skin effect and strong coupling superconductivity. It has been demonstrated, however, that the full theory is not strictly necessary, that the simpler, and more generally applicable, theory due to Allen is sufficiently accurate to be useful in interpreting the experimental results.

Using the simple theory as a guide, the experimental spectrum for lead has been inverted to yield a phonon density of states. This density of states differs from that derived from superconducting tunneling experiments in two ways. Firstly, the main phonon peaks are broader than indicated by the tunneling results. This is probably due to the weaknesses of the simple theory. Secondly, the density of states derived here contains considerable fine structure not evident in the tunneling measurements. Most of this structure is, however, contained in the density of states derived from

inelastic neutron scattering and can, therefore, be believed. In particular, a peak corresponding to phonons of energy close to the superconducting gap energy 2Δ is taken as direct evidence of the influence of the superconducting transition on the phonon spectrum. There is a 1 cm^{-1} discrepancy in phonon peak energies between the neutron and tunneling densities of states. Again this work agrees with the neutron results.

Strong phonon structure has also been found in two weaker coupling superconductors, indium and niobium. Here, surprisingly, the simple theory seems less applicable than in the case of lead. The breakdown of the simple theory manifests itself primarily as a shift in the positions of the phonon peaks. A partial explanation of this breakdown has been presented and a systematic variation in the shift from material to material has been observed. This empirical relationship between the frequency shift and two material parameters, the Debye frequency and the energy gap, should be useful in the study of new materials, enabling the frequencies of phonon peaks to be established within a few percent, despite the breakdown of the theory.

These results, along with weaker evidence of phonon structure in mercury and Nb_3Sn , indicate that general applicability of the technique is to be expected as experimental methods are improved.

APPENDIX

An inherent problem in Fourier transform spectroscopy is that the noise is transformed along with the signal. Thus, unless the noise is "white", the noise level will vary across the spectrum making it difficult to decide which structure in the spectrum is real and which is due to noise. Real structure in one part of the spectrum may be dismissed as erroneous because it is smaller than what is obviously noise in another region of the spectrum. Alternatively, a noise source may be persistent and of a well defined frequency giving rise to an erroneous peak, on an otherwise quiet spectrum, which is reproducible from scan to scan. Confusion may also occur if there are noise sources that primarily affect the region of the interferogram close to the zero path difference position. These can give errors in the spectrum that vary slowly with frequency, producing a large overall noise level, while sharper and much smaller structure evident in the spectrum is in fact real.

Of primary concern in these experiments are noise sources that give oscillations in the spectrum of period comparable to the width of the phonon peaks, 30 to 50 cm^{-1} .

However, much sharper noise can be important when, as in lead, the phonon spectrum has fine structure. Also noise sources that add a smooth background to the spectrum can indirectly give structure that may be confused with the phonon spectrum. This is because real but irrelevant structure in the spectrum will not divide out when a ratio is taken of two spectra, each with a different erroneous background.

In sections 1, 2, and 3 the effects of the most important sources of noise are discussed. In section 4 the method of averaging many spectra to minimize the noise is described. An estimate of the total noise expected on the final spectrum is quoted in section 5.

1. Electrical Noise

Random electrical noise is always present on the interferogram to a level of at least 100 nV RMS. About half of this can be attributed to Johnson noise from a 5 megohm bias resistor at room temperature. The remaining 50 nV of noise is due to a variety of sources that can be minimized but never completely eliminated. These include poor electrical contact to the detector, mechanical vibrations of detector leads, and noise inherent in the mercury cells used as a bias voltage source.

Typically signal strengths are 0.1 to 1 mV so the electrical noise level on the interferogram is about 0.1%. Since this source of noise is essentially random its effect on the spectrum is again random noise, across the whole spectrum,

of about 0.1%. This can be further reduced by averaging of many spectra and is the least problematic source of error.

2. Lamp Fluctuations

The light source used in these experiments, the Hg arc lamp with a quartz envelope, gives greater intensity below about 250 cm^{-1} than the glow bar or tungsten filament which are also used in infrared sources, but suffers the disadvantage of instability. The instability is not random but usually takes the form of sudden fluctuations between two relatively stable levels of intensity. The noise on the interferogram is then an irregular square wave with a period 10 to 100 s. Since the interferogram is usually sampled at one data point per second the primary effect of these fluctuations is on spectral components below 20 cm^{-1} , but the rapid transition from one level to the other causes noise across the whole spectrum. The size of the intensity fluctuations varies from lamp to lamp, and even from day to day with the same lamp, being at best 0.1% of the total intensity and frequently 1 or 2%.

Noise from the lamp instability is to a large extent eliminated by the double beam operation of the interferometer. The double beam system, however, has two major drawbacks. Firstly, using half the light intensity as a reference beam reduces the signal size by a factor of two. A further reduction is caused by the waveform being no longer a square wave and by the shadowing effect of the chopper shaft. The total loss in signal is then about a factor of three,

whereas the electrical noise level remains constant. Double beam operation is then only useful if lamp fluctuations are the dominant source of noise by at least a factor of three.

The second drawback is that the lamp fluctuations are not eliminated in the region of the interferogram near zero path difference where the net signal is comparable to the total signal. The effect of noise in this region of the interferogram is to give smooth oscillations across the spectrum while leaving the details of fine structure relatively unaffected. The double beam operation, then, while useful for measuring fine structure in the phonon spectrum, still permits large errors that influence overall spectral shape.

3. Stepping Errors

Ideally the interferogram should be sampled at equally spaced intervals of path difference. Also, if electronics with a significant time constant is used to average the signal, the sampling should occur at equally spaced intervals of time. The original drive in the Michelson interferometer employed a lead screw and nut driven continuously by a synchronous motor through plastic gears. Such an arrangement inevitably led to "slip-stick" motion and a highly variable velocity. The time between read pulses produced by a Moire fringe system varied by 10%. This timing error is equivalent to a position error of comparable size.

Conversion to a stepping motor system rated for speeds up to 300 steps/s reduced the timing errors to less than 0.3% with a stepping interval of 1 s. This then left

position errors due to the stepping motor of 2 μ /step and due to the commercial drive stage of about 1 μ /step. Thus, the expected inaccuracy in position on a 500 cm $^{-1}$ cutoff run is 1.5%.

The effect of this residual error on the spectrum can be seen from the following calculation. Consider an ideal double sided interferogram $V(x)$ sampled at path difference points equally spaced Δx apart. The true interferogram is then a set of points

$$V_n = V(n\Delta x) \quad n = -N, \dots, 0, \dots, N$$

Fourier transforming gives the true (complex) spectrum

$$(1) \quad A_k = \sum_{n=-N}^{+N} V_n e^{-i\pi nk/N} \quad k = -N \dots, +N$$

and the inverse Fourier transform

$$(2) \quad V_n = \frac{1}{2N+1} \sum_{m=-N}^{+N} A_m e^{i\pi mn}$$

Suppose that stepping errors cause the actual position after the n th step to be $n\Delta x + dx_n$ then the actual interferogram is, to first order in $dx_n/\Delta x$

$$(3) \quad V'_n = V_n + \frac{dV_n}{dx} dx_n$$

with the Fourier transform

$$(4) \quad A'_k = \sum_{n=-N}^N V'_n e^{-i\pi nk/N}$$

Differentiating equation (2) with respect to $x=n\Delta x$

$$(5) \quad \frac{dV_n}{dx} dx_n = \frac{i\pi}{2N+1} \sum_{m=-N}^N \frac{m}{N} \Lambda_m \frac{dx_n}{\Delta x} e^{i\pi mn/N}$$

and substituting equations (1), (2), (3) and (5) into equation (4)

$$(6) \quad \Lambda_k = \Lambda_k + \delta\Lambda_k$$

$$(7) \quad \delta\Lambda_k = \frac{i\pi}{2N+1} \sum_{m=-N}^N \frac{m}{N} \Lambda_m \sum_{n=-N}^N \frac{dx_n}{\Delta x} e^{-i\pi n(k-m)/N}$$

Assuming for simplicity that the true interferogram is perfectly centered then $\Lambda_{-m} = \Lambda_m = |\Lambda_m|$ and equation (7) becomes

$$(8) \quad \delta\Lambda_k = \frac{i\pi}{2N+1} \sum_{m=0}^N \frac{m}{N} |\Lambda_m| \sum_{n=-N}^N \frac{dx_n}{\Delta x} (e^{-i\pi n(k-m)/N} - e^{-i\pi n(k+m)/N})$$

The amplitude spectrum calculated from the actual interferogram is

$$(9) \quad |A'_k| = [A'_k A'_{-k}]^{1/2} = |A_k| \left\{ 1 + \frac{\delta\Lambda_k + \delta\Lambda_{-k}}{|A_k|} \right\} \quad k = 0, 1, \dots, N$$

Therefore, from equation (8)

$$(10) \quad |A'_k| = |A_k| \left[1 + \frac{\pi}{2N+1} \sum_{m=0}^N \frac{m}{N} \frac{|A_m|}{|A_k|} \{E_{k-m} - E_{k+m}\} \right]$$

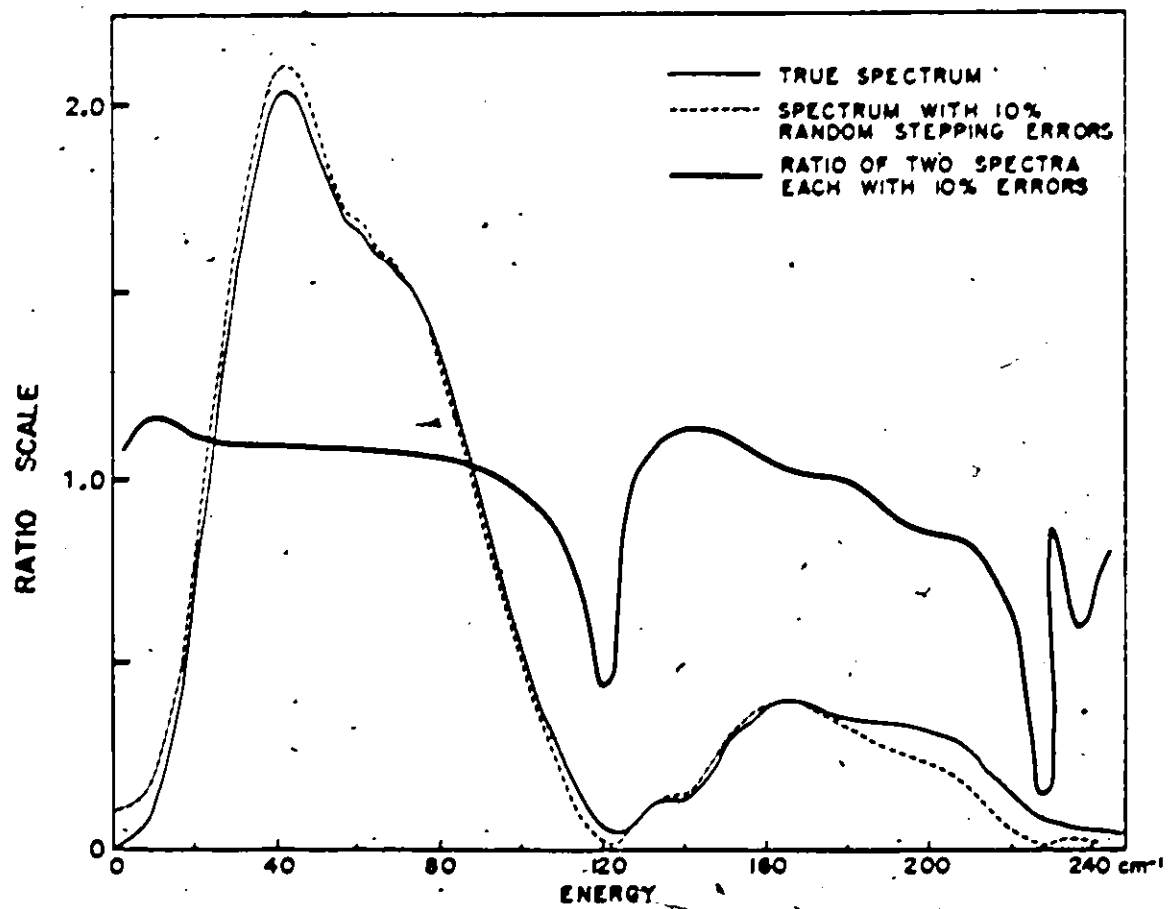
where E is the sine Fourier transform of the stepping errors

$$(11) \quad E_\ell = \sum_{n=-N}^N \frac{dx_n}{\Delta x} \sin\left(\frac{\pi \ell n}{N}\right)$$

Figure (21) shows the effect on a spectrum of stepping errors randomly distributed on the interval $\pm 10\%$, calculated according to equation (10). This is an extreme example but serves to demonstrate the smooth background that

FIGURE 21

The effect of stepping errors on a spectrum. The size of the errors in this calculation is extreme but the graphs demonstrate the kind of structure that is introduced into the spectrum by random stepping errors.



that is added to the spectrum in the presence of random error. The magnitude of the background is about 5% of the peak intensity so that even in the more realistic case of a 1 or 2% error the effect is significant.

Figure (21) also shows the ratio of the same spectrum with the two different sets of random errors present to the level of 10%. The region of the curve above 100 cm^{-1} clearly shows that the stepping errors can give structure in the spectrum of width of the order of 50 cm^{-1} . In a more realistic case the structure would be reduced by a factor of 10 but even so would be significant in relation to real, phonon induced, structure.

4. Signal Averaging

The signal to noise ratio on a single fast scan could be improved by as much as a factor of 10 by signal averaging, the limit being set by the time available before the He^4 or He^3 ran out.

Signal averaging can take the form of scanning slowly with a long time constant or averaging together many fast scans. If the noise is purely random the two methods are almost equivalent but the former is inappropriate to both lamp fluctuations and stepping errors. This is because the lamp fluctuations are of period much longer than a time constant and, obviously, the time constant has no effect on the positional accuracy of the mirror drive.

The averaging together of many scans is, therefore,

the preferred technique but has the inherent difficulty that the noise on amplitude spectra will not average to zero, but to its RMS value. This can be shown as follows.

The sine and cosine coefficients of a double sided transform can be represented as a two dimensional vector $S(v)$, for each frequency v . This vector will be the sum of the vectors representing the true spectrum, $S_T(v)$, and the noise, $N(v)$.

$$(12) \quad \vec{S}(v) = \vec{S}_T(v) + \vec{N}(v)$$

The average of many amplitude spectra is then

$$(13) \quad \langle |\vec{S}(v)| \rangle = \langle |\vec{S}_T(v) + \vec{N}(v)| \rangle$$

Expanding equation (12)

$$(14) \quad \begin{aligned} \langle |\vec{S}(v)| \rangle &= \langle [S_T^2 + 2\vec{S}_T \cdot \vec{N} + N^2]^{1/2} \rangle \\ &= \langle [S_T^2 + 2\vec{S}_T \cdot \vec{N} + N^2]^{1/2} \rangle \end{aligned}$$

The approximation is valid if the noise is small.

Thus

$$(15) \quad \langle |\vec{S}(v)| \rangle = \langle [S_T^2 + 2\vec{S}_T \cdot \vec{N} + N^2]^{1/2} \rangle$$

The first term on the right hand side of equation (15) gives the true spectrum, $S_T(v)$. Since the angle between \vec{S}_T and \vec{N} will be random, the second term will average to zero. The third term, however, is strictly positive and will average to the mean square value of the noise.

One wishes, therefore, to average the scans before

taking the modulus

$$|\langle \vec{S}(v) \rangle| = |\langle \vec{S}_T(v) \rangle + \langle \vec{N}(v) \rangle|$$

This is accomplished by the following procedure.

For each scan, first $S(v)$ is determined from the sine and cosine coefficients of the full interferogram. A noise free, but low resolution, estimate of the phase of $S_T(v)$ is then made by transforming a few points on either side of the central maximum. The assumption here is that the phase of $S_T(v)$ is a smooth function of frequency. The vector $S(v)$ is then rotated through an angle equal to the phase of $S_T(v)$ so that the contribution of $S_T(v)$ to $S(v)$ is at zero phase for each scan. The scans can be added together vectorially and, lastly, the modulus taken to give the amplitude spectrum. Since a vector, rather than an algebraic, average is taken, the noise will average to zero after many scans.

This technique is similar to that developed by Mertz (1967) for the phase correction of single sided transforms but no assumption has been made concerning the symmetry of the interferogram.

5. Total Noise

Each of the three sources of noise is expected to give a noise level on the derivative of a single spectrum of about 0.001 cm. (The spectrum is taken to be dimensionless and of the order of 1. The units of the derivative, with the energy measured in cm^{-1} , are then cm.) The electrical noise

is expected to be essentially white but the other two sources are expected to give oscillations across the spectrum of period of 30 cm⁻¹ and longer. When these are combined and account taken of averaging, typically, 25 scans and of taking a ratio the final noise level expected on the derivative is 0.0005 cm. The observed structure in niobium, for instance, has an amplitude of about 0.003 cm, giving a signal to noise ratio of 6. This is consistent with the noise level observed in figure (16), although the noise is not uniformly distributed across the spectrum.

In the case of lead the structure is stronger by a factor of 10 so the noise level is 1 or 2%.

V

BIBLIOGRAPHY

- Allen, P. B. 1970. Phys. Rev. B 3, 305
- Anderson, J. R. and Gold, A. V. 1965. Phys. Rev. 139, A1459
- Axe, J. D. and Shirane, G., 1973. Phys. Rev. B 8, 1965
- Bermon, S. and Ginsberg, D. M. 1964. Phys. Rev. 135, A306
- Blackford, B. L. and March, R. H. 1968. Can. J. Phys. 46,
141
- Blackford, B. L. and March, R. H., 1969. Phys. Rev. 186, 397
- Brandli, G. and Sievers, A. J. 1972. Phys. Rev. B 5, 3550.
- Carbotte, J. P. 1975. Private Communication
- Chantry, G. W. 1971. Submillimetre Spectroscopy (Academic
Press, London and New York)
- Coulthard, M. A. 1973. Private Communication
- Douglass, R. J. and Timusk, T. 1974. Applied Optics 13, 723
- Drew, H. D. and Sievers, A. J. 1969. Applied Optics 8, 2067
- Dynes, R. C. and Narayanamurti, V. 1972. Phys. Rev. B 6, 143
- Gavini, A. and Timusk, T. 1971. Phys. Rev. B 3, 1049
- Ginsberg, D. M. 1966. Phys. Rev. 151, 241
- Glover, R. E. and Tinkham, M. 1957. Phys. Rev. 108, 243
- Joyce, R. R. and Richards, P. L. 1970. Phys. Rev. Lett. 24,
1007
- Mattis, D. C. and Bardeen, J. 1958, Phys. Rev. 111, 412

- McMillan, W. L. and Rowell, J. M. 1969. In Superconductivity ed. by R. D. Parks (Marcel Dekker, New York), Vol. 1, p.561
- Mertz, L. 1967. Infrared Physics 7, 17
- Nakagawa, Y. and Woods, A. B.D. 1963. Phys. Rev. Lett. 11, 271
- Nam, S. B. 1967. Phys. Rev. 156, 470, 487
- Norman, S. L. 1968. Phys. Rev. 167, 393
- Palmer, L. H. and Tinkham, M. 1968. Phys. Rev. 165, 558
- Reuter, G. E. and Sondheimer, E. H. 1948. Proc. Roy. Soc. (London) A195, 336
- Richards, P. L. and Tinkham, M. 1960. Phys. Rev. 119, 575
- Rowell, J. M. and Dynes, R. C. 1971. Proc. Int. Conf. on Phonons, Rennes, France
- Schuster, H. G. 1973. Solid State Commun. 13, 1559
- Shen, L.Y.L. 1972a. In Superconductivity in d- and f-band Metals. ed. by D. H. Douglass (American Institute of Physics, New York)
- Shen, L.Y.L. 1972b. Phys. Rev. Lett. 29, 1082
- Stedman, R., Almquist, L. and Nilsson, G. 1967. Phys. Rev. 162, 549
- Swihart, J. C. and Shaw, W. 1971. Physica 55, 678
- Tomlinson, P. G. and Carbotte, J.P. 1974. Private Communication
- Tumber, A. J. 1968. M. Sc. Thesis, McMaster University